Earth-Science Reviews 268 (2025) 105173

Contents lists available at ScienceDirect

Earth-Science Reviews

journal homepage: www.elsevier.com/locate/earscirev

Review Article

Soil bulk density and porosity connecting macro- and micro-scales through geometry.

D.A. Robinson [a,*], S.P. Friedman [b], A. Thomas [a], D. Hirmas [c], P.L. Sullivan [d], A. Nemes [e,f]

[a] UK Centre for Ecology & Hydrology, Environment Centre Wales, Bangor, UK
[b] The Institute of Soil, Water and Environmental Sciences, Agricultural Research Organization, Volcani Center, Rishon LeZion 7505101, Israel
[c] Department of Plant and Soil Science, Texas Tech University, Lubbock, TX, USA
[d] College of Earth Ocean and Atmospheric Science, Oregon State University, OR, USA
[e] Faculty of Environmental Sciences and Natural Resource Management, Norwegian University of Life Sciences, Ås, Norway
[f] Division of Environment and Natural Resources, Norwegian Institute of Bioeconomy Research, Ås, Norway

ARTICLE INFO

Keywords:
Grain
Packing
Shape
Soil
Granular media
Particle size distribution

ABSTRACT

Soil bulk density (BD) is a macroscopic indicator frequently used to infer the soils' pore system, a fundamental attribute of terrestrial environments that significantly affects processes such as infiltration, water retention and plant root development. Additionally, BD is essential for assessing the storage of various materials in soils and sediments, including carbon and nutrients. High bulk density, often a consequence of soil compaction, represents a form of soil degradation that diminishes the soil's functional capacity. Therefore, effective management of soil BD is crucial for improving agricultural yields, safeguarding ecosystem services, preventing degradation, and preserving the overall integrity of the Earth's system. This review synthesizes recent research on the packing behavior of granular materials to clarify the emergent property of soil BD. The findings yield an empirical model that links packing fraction to the shape and size ratio of particles. The results demonstrate that the model accurately captures the frequently observed exponential decrease in soil BD with increasing soil organic matter (SOM) content. While it is widely recognized that particle density influences BD, the analysis indicates that grain shape exerts a considerable effect, followed by the particle size ratio in granular media. The insights from this study aim to transform the perception of BD from a static notion to one that acknowledges how changes in the morphology of soil constituents, driven by factors such as root growth and decomposition, can result in variations in BD. As a result, BD may become increasingly sensitive to feedback from climate and land use changes as the geometry of SOM evolves.

Contents

* Corresponding author.
E-mail address: David.Robinson@ceh.ac.uk (D.A. Robinson).

https://doi.org/10.1016/j.earscirev.2025.105173
Received 22 July 2024; Received in revised form 7 March 2025; Accepted 23 May 2025
Available online 25 May 2025

1. Introduction

The soils' pore system, often characterized by soil bulk density (BD), plays a crucial role in the movement of mass and energy within soils, and is largely influenced by the arrangement of soil grains (Dippenaar, 2014; Flint and Flint, 2002; Grossman and Reinsch, 2002; Nimmo, 2004). Furthermore, Hirmas et al. (2018) have identified significant continental-scale variations in macroporosity over decadal periods, which may have unknown implications for hydrological processes. Additionally, bulk density is vital for assessing carbon and moisture reserves in soils (Kravchenko et al., 2019; Lee et al., 2009; Xu et al., 2016). Increasingly, soils face threats from a cycle of compaction, heightened runoff, and erosion resulting from management practices. While the effects of escalating erosion are evident (Borrelli et al., 2017), the fundamental mechanisms driving changes in soil bulk density at the grain level remain inadequately understood.

Bulk density is fundamentally an emergent physical property. A comprehensive understanding of this property necessitates investigation that elucidates the bulk property through the emergent behavior of its grain- or micro-scale components (Tranter et al., 2007). From a macroscopic viewpoint, extensive datasets concerning soils and sediments consistently indicate a exponential reduction in bulk density as soil organic matter (SOM) increases (Atwood et al., 2020; Avnimelech et al., 2001; Hossain et al., 2015; Keller and Håkansson, 2010; Koop et al., 2023; Ramcharan et al., 2017; Reynolds et al., 2013; Ruehlmann and Körschens, 2009). Nevertheless, the mechanisms that govern this phenomenon are not thoroughly understood from a grain scale perspective. By employing such an approach to investigate the properties of grain assemblies based on the shape and size distribution of their particles, significant physical insights into the emergence of soil structure can be obtained, which may not be apparent from macroscopic assessments. Such insights could enhance our comprehension of soil grain packing and their susceptibility to compaction, as well as the influence of plants and other organisms in mitigating this compaction.

It is suggested that the commonly observed decrease in soil bulk density, which correlates with an increase in soil organic matter (SOM), is affected by the particle densities of the components within the mixture, along with their particle shape and size distribution. Therefore, our objectives are to, i) synthesize the recent literature on the packing of granular media; ii) apply insights from the granular media literature to soil physics to enhance the description and comprehension of soil bulk density. To achieve these aims, this work is organized as follows, 1. Introduction, 2. Macroscopic packing and bulk density; 3. Packing of monosized hard spheres; 4. Packing of monosized grains of different shapes; 5. Particle size distribution and binary mixtures; 6. Inter-particle forces; 7. Modeling the packing of granular media; 8. Modeling the bulk density of soils before 9. General Discussion. This discussion will address the implications for soil management and restoration based on the insights obtained. The outlined objectives will not only deepen our understanding of the emergent packing behavior but will also aid in developing a structural model that underpins various other physical properties, including electrical, thermal, and hydrological characteristics (Kojima et al., 2018).

2. Macroscopic packing and bulk density

The arrangement of spheres has been a subject of study for centuries due to the significance of object packing in science and industry (Aste and Weaire, 2008; Conway and Sloane, 2013; Cumberland and Crawford, 1987; Hales et al., 2017; Kepler, 1966; Torquato, 2013; Torquato and Stillinger, 2010; Weitz, 2004; Zong, 2008). Expanding the focus from spherical to non-spherical particles is crucial for accurately describing and comprehending the behavior of natural materials. This is particularly relevant for soils and sediments (Robinson et al., 2022), which frequently consist of platy or fibrous particles. Establishing a link between the macroscopic measurement of bulk density and the microscale properties of the soil can provide significant physical insights. Bulk density serves as a vital state parameter in the field of earth sciences (Blake and Hartge, 1986; Grossman and Reinsch, 2002). The packing of granular particles in nature leads to the macroscopic – bulk relationship between porosity (φ, $m^3\ m^{-3}$), bulk density (ρ_b, $kg\ m^{-3}$), particle density

Table 1
Packing fractions of hard spheres in lattice structures or organized configurations, modified from (Cumberland and Crawford, 1987). Other ordered configurations are presented in the reference for z = 11 η = 0.7183; then, 9, 0.6134; 7, 0.5612; 5, 0.4031; 3, 0.2234; 2, 0.0545.

Packing group	Common name	Analytical expression	Packing fraction η ($m^3\ m^{-3}$)	Number of contacts (z)
Rhombohedral	Face-centered cubic FCC (pyramidal)	$\pi/(3\sqrt{2})$	0.7405	12
Rhombohedral	Hexagonal close-packed HCP (clear passage)	$\pi/(3\sqrt{2})$	0.7405	12
Rhombohedral	Rhombohedral (blocked passage, twinned)	$\pi/(3\sqrt{2})$	0.7405	12
Tetragonal Sphenoidal	Tetragonal Sphenoidal (clear passage)	–	0.6981	10
Tetragonal Sphenoidal	Tetragonal Sphenoidal (Blocked passage)	–	0.6981	10
Orthorhombic	Orthorhombic, (blocked passage)	$(\pi\sqrt{3})/8$	0.6801	8
Orthorhombic	Orthorhombic, (clear passage)	$\pi/(3\sqrt{3})$	0.6046	8
Orthorhombic	Orthorhombic, cubic tetrahedral (BCC)	$\pi/(3\sqrt{3})$	0.6046	8
Simple cubic lattice	Simple cubic (SC)	$\pi/6$	0.5236	6
Tetrahedral lattice	Diamond cubic	$(\pi\sqrt{3})/16$	0.3401	4

(ρ_s, kg m^{-3}), and packing fraction (η, m^3 m^{-3}), Eq. (1):

$$\varphi = 1 - \left(\frac{\rho_b}{\rho_s}\right) = (1 - \eta) \quad (1)$$

It is both scientifically and practically intriguing to comprehend the mechanisms by which particles aggregate to create a macroscopic structure. Consequently, the investigation into the emergence of bulk density or porosity can adopt a stereoscopic perspective, encompassing both microscopic and macroscopic dimensions (Scarlett et al., 1998).

3. Packing of monosized hard spheres

The microscopic perspective commences with an analysis of the packing behavior of monosized hard (non-overlapping) spheres. This issue holds significant relevance in the fields of crystallography, chemistry, physics, and materials science, making it a thoroughly researched topic (Conway and Sloane, 2013). The packing fraction (η) of spheres within lattice structures is well-known and described quantitatively in Table 1.

A more complex issue lies in comprehending and articulating the packing behavior of disordered systems composed of monosized spheres. In their study, Song et al. (2008) provided a mathematical framework to determine the packing fraction of monosized hard spheres in both random loose packing (RLP) and random close packing (RCP) scenarios. Their model established a relationship between the packing fraction and the coordination number, denoted by the symbol ⟨C⟩, which represents the average number of contacts in random packings. They formulated an equation of state for the packing fraction ($\eta = 1\text{-}\varphi$) that is contingent upon the number of contacts, or ⟨C⟩:

$$\eta \approx \frac{\langle C \rangle}{\langle C \rangle + 2\sqrt{3}} \quad (2)$$

According to Eq. (2), in the context of the maximally random jammed (MRJ) state characterized by an average coordination number of ⟨C⟩ = 6, the researchers determined that the packing fraction η is 0.634 (m^3 m^{-3}) for frictionless particles (with a coefficient of friction $\mu = 0$). Conversely, for the maximally jammed loose state, where ⟨C⟩ = 4, the packing fraction η was found to be 0.536 (m^3 m^{-3}) as the coefficient of friction approaches infinity ($\mu \to \infty$). This study lays the groundwork for subsequent theoretical investigations that extend beyond spherical particles to include those of various geometrical shapes.

3.1. Contact, kissing, and coordination numbers

The contact number, defined as the ratio of the total number of contacts within a packing to the total number of particles, serves as a valuable metric for characterizing the spatial arrangement of random packing (Bernal and Mason, 1960; Bezdek and Khan, 2018). Strong relationships have been found between packing fraction (η) and contact number in disordered packing (Migal et al., 2020). Furthermore, the contact number plays a crucial role in understanding the physical properties of materials. It encompasses aspects such as strength, the transfer of forces through force chains, and the overall stability of a packing structure. This may explain the enduring fascination this issue has held for scientists over the centuries.

In 1611, Johannes Kepler posited that *no packing of congruent balls in Euclidean three-space has a density greater than that of the face-centered cubic packing*. This assertion, known as the Kepler conjecture (Kepler, 1966), remained unproven until a recent proof by exhaustion (Hales et al., 2017). Subsequently, in 1694, a notable exchange took place between Isaac Newton and David Gregory. It was concerning, *how many spheres can be placed around a given sphere, such that they are all the same size and touch the central one*. This quantity is referred to as the '*kissing number*' determined by the optimal arrangement of spheres to maximize contact with the central sphere. In mathematical terms the *kissing number* k(n) also known as the *Newton number* represents the highest number of non-overlapping spheres that can simultaneously touch another sphere of the same size; for three dimensions (d = 3) this number is 12 (Table 1) (Conway and Sloane, 2013). Newton advocated for the number 12 while Gregory proposed 13; although 12 is the correct answer, it may seem counterintuitive, as it is possible to tightly pack 13 spheres around a central sphere, albeit not all will make contact (Anstreicher, 2004; Aste and Weaire, 2008). In lattice packings, each sphere touches the same number of neighboring spheres, a condition that does not hold true for disordered packings.

In disordered packings, the term used to describe the number of contact points is referred to as the *contact number* (*z*) or the average contact number ⟨C⟩, also known as the *coordination number* (CN), or *ligancy* within the field of material science. Additional relevant concepts include the *local coordination number*, which considers nearby spheres that do not make contact with a central sphere; this may encompass spheres located in a second coordination shell (Migal et al., 2020). Other significant coordination numbers include the *caging number* which is approximately 4.71 and the *parking number* which is around 8.7. The caging number represents, '*the average minimum number of randomly placed particles required to block all movement of a center particle*' (Wouterse, 2008); whereas the parking number for spheres denotes, '*the average of the maximum number of particles that can be placed randomly on a central particle without interpenetration of the surrounding particles with each other*' (Wouterse, 2008). Consequently, the parking number serves

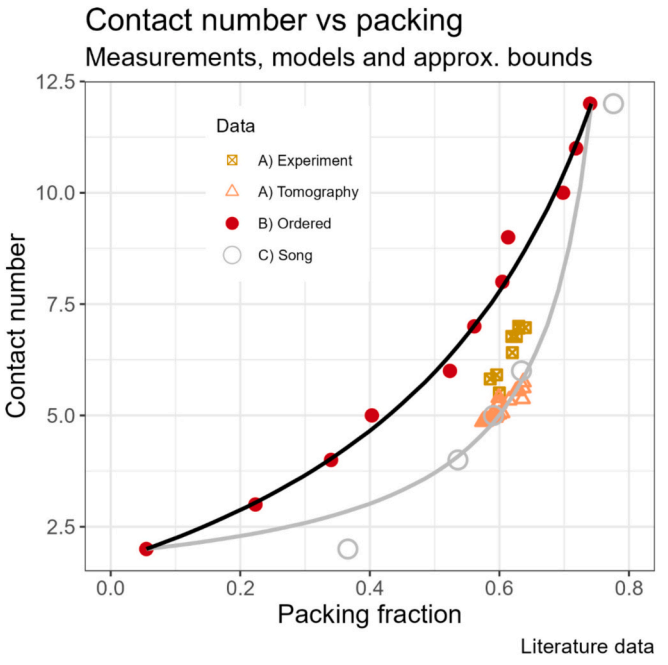

Fig. 1. Illustrates the relationship between contact numbers and packing fraction for both measured monosized disordered sphere packings (represented by non-circles) and modeled ordered and disordered sphere packings (depicted as circles). The values for ordered packing (indicated by red circles) are sourced from the works of (Cumberland and Crawford, 1987; Manegold and von Engelhardt, 1933) with the number of contacts equal 2 at the low end and 12 at the upper end. The large open grey circles denote model predictions for MRJ spheres, as discussed by (Song et al., 2008). Notably, these predictions diverge from the expected range of 0.54 to 0.64 when extended into the dilute range of 0.36, as indicated by the grey line. The black and grey lines serve as approximate upper (black line for ordered packing) and lower (grey line for disordered packing) bounds, which have been fitted using the proposed empirical function (Eq. (3)). The measurement data, represented by triangles, originates from experimental packings obtained through tomography, as reported by (Delaney et al., 2010). Additionally, the yellow crossed squares represent measurements derived from packing experiments and contact counting found in the literature, specifically from (Aste et al., 2005).

as a less stringent limit compared to the kissing number.

The correlation between the quantity of contacts and packing density warrants investigation. This can be achieved by analyzing precise values for lattice configurations alongside empirical data derived from either real-world or computational experiments involving spheres in a maximally jammed random state. The information presented in Fig. 1 and Table 1 offers significant insights into lattice structures and the most efficient packing arrangements (Cumberland and Crawford, 1987; Manegold and von Engelhardt, 1933). The analysis of these lattices reveals that the association between the number of contacts and packing fraction is not singular; for instance, body-centered cubic (BCC) and hexagonal close packing exhibit identical contact numbers yet differ in their packing fractions. Furthermore, it is noteworthy that various structures can coexist at the same packing fraction; for example, face-centered cubic (FCC) and hexagonal close packing (HCP) share the same packing fraction (η) and contact number, ($z = 12$), but they are arranged differently.

Disordered arrangements of spheres, referred to as maximally random jammed configurations (Torquato et al., 2000), exist at the extremes of packing fractions known as random close-packed (RCP) and random loose-packed (RLP). The experimental determination of contact numbers poses significant challenges, as spheres may be nearly in contact without actually touching, leading to potential overestimation of contacts. Additionally, many mathematical models operate under the assumption that spheres are frictionless, a condition not typically met in practical experiments. Considering these complexities, the findings regarding maximally jammed spheres, derived from a synthesis of experimental data compiled by Aste et al. (2005) are illustrated in Fig. 1, which incorporates measurements from earlier studies (Bernal and Mason, 1960; Mason, 1968; Scott, 1962) represented by open crossed squares. Recent advancements in measurement methodologies and computational simulations have further enhanced the accuracy of these measurements. Delaney et al. (2010) employed a hybrid approach utilizing X-ray computed tomography (XCT) alongside discrete element method (DEM) simulations to analyze the properties of sphere packings. This investigation included the average contact number, denoted as ⟨C⟩ for spheres in a maximally random jammed state (Fig. 1, open triangles). Furthermore, the integration of empirical experiments with DEM simulations allowed for adjustments related to friction, providing insights into its influence on packing characteristics. The refined experiments conducted on gravitationally packed spheres yielded results that were lower than those from previous studies, indicating prior overcounting of contacts, while revealing that the impact of friction on the examined packings was minimal.

The significance of the physical relationship between η and z *or* ⟨C⟩ in determining material properties, particularly mechanical stability, has led to substantial efforts in modeling this relationship. Migal et al. (2020) presented a compilation of equations aimed at empirically representing the connection between η and z or ⟨C⟩ for both ordered and disordered sphere packings. The findings from the models utilized in their study reveal a lack of consistent predictive accuracy for both ordered and MRJ packings. This underscores the complexity of the issue, particularly with the inclusion of disordered packings.

Song et al. (2008) introduced Eq. (2) to describe disordered sphere packing, establishing a relationship between the average coordination number ⟨C⟩ and the packing fraction, η. The density of approximately 0.64, commonly known as the random close packing (RCP) limit, is influenced to some degree by the specific method employed to achieve the packing configuration (Torquato et al., 2000). This observation carries significant implications for the interpretation of computer simulations that utilize various techniques to generate packing arrangements. The outcomes of Eq. (2) are illustrated in Fig. 1 as open circles, with values extrapolated beyond the disordered range to $z = 2$ and 12, to analyze the behavior at these extreme limits. The findings demonstrate a strong correlation with the data within the loose and close-packed boundaries (0.54–0.64), although the correspondence diminishes outside these ranges, as anticipated.

The findings derived from both experimental and model analyses (see Fig. 1) indicate that lattice structures typically establish an upper limit. Disordered packings, specifically Random Loose Packing and Random Close Packing, exhibit greater density compared to their tetrahedral and simple cubic lattice counterparts, given an equivalent number of contacts. The existence of two distinct packing fractions for $z = 8$ implies that a singular relationship does not exist. This observation indicates a range of potential combinations of z and η which are influenced by various forces and steric considerations. While some researchers have suggested empirical equations, such as those proposed by Pabst and Gregorova (2007), testing these equations across all lattice types revealed that the equation ($z = \pi/(1\text{- }\eta)$ was unreliable at lower packing fractions and did not account for a lower bound. Consequently, further exploration of equations was undertaken to identify an appropriate empirical representation for the bounds. A function finder tool (findcurves.com) was employed, yielding numerous candidates; however, the majority of these functions exhibited multiple coefficients that demonstrated erratic behavior concerning both the upper and lower bounds.

We suggest an equation structured in the following manner to effectively represent the behavior of the spheres and establish approximate limits. The mean contact number ($\langle C\rangle_B$) can be described by this well-behaved empirical formula, requiring a single unknown fitting parameter (β).

$$\langle C\rangle_B = \langle C\rangle_k + (1 - f_n)\,\langle C\rangle_k \left(\frac{\langle C\rangle_l - \langle C\rangle_k}{\langle C\rangle_k + f_n \times \beta\left(\langle C\rangle_l - \langle C\rangle_k\right)} \right) \tag{3}$$

In this context, the variable, $\langle C\rangle_k$ represents the number of contacts corresponding to the maximum packing density (0.74), which is quantified as 12, also known as the kissing number. Conversely, $\langle C\rangle_L$ denotes the number of contacts, 2, associated with the minimum packing density of 0.055 (Gardner, 1966). The normalized packing fraction, denoted as f_n ranges from 0 to 1. To align with the actual bounds of the packing fraction, which span from 0.055 to 0.74, the x-axis was modified accordingly.

$$\eta = f_n(0.74 - 0.055) + 0.055 \tag{4}$$

The findings for this model are illustrated in Fig. 1, where the solid black line, representing $\beta = 0.75$, serves as an approximate upper limit, while the grey dashed line, corresponding to $\beta = 1.07$, indicates an approximate lower limit. The grey line aligns with the results presented by Song et al. (2008) and the empirical data concerning disordered packings. The equation for $\langle C\rangle_B$ delineates a region within which the combinations of $\langle C\rangle_B$ and η are expected to be situated.

Aste et al. (2005) emphasize that the contact number is a poorly defined experimental parameter. Variability in the geometry of manufactured spheres and the positioning of their centers results in imprecise counts of contact numbers in experimental packings. In their study, Table 1 in Aste et al. (2005) illustrates the variation in contact number (n_t) as the radial distance (r) increases from (r) = 1.02 to 1.1 times the particle diameter (⌀). The data indicate low contact numbers at r (1), but within the measurement precision, ($r = 1.02$) yields a value of n_t of approximately 6, contingent on η. This value escalates significantly with distance, n_t reaching about 8 at ($r = 1.1$), which is an increase of roughly 2. Although the contact number is experimentally ill-defined, it remains a crucial parameter for practical applications and theoretical investigations, particularly concerning mechanical behavior. Furthermore, it has been demonstrated that the average contact number ⟨C⟩, for a specific η, is influenced by the method of packing and the level of order, whether isotropic or anisotropic. Literature values for physically packed random close packing include 6.4 (Bernal and Mason, 1960), for shaken ball bearings with the number approximately 1000; 6.24 (Pinson et al., 1998) for ball bearings; 3.7, 6.9 or 7.7 depending on assumptions about contact and voxel size (Aste et al., 2004), derived from XCT

imaging of poured, tapped, compressed spheres with the number around 20,000; further improvement gave a value of about 5 (using the improved hybrid method) (Delaney et al., 2010) through tomographic imaging of acrylic beads and discrete element method (DEM) simulations; and approximately 5.6 (Sibellas et al., 2024) for 1 mm glass beads via X-ray microtomography. Values derived from computer simulations of the random close packing include 6.0 as reported by (Bennett, 1972), using a sequential addition algorithm; 5.99 as noted by Matheson (1974), utilizing the "drop and roll" addition technique; 6.0 as reported by Liu et al. (1999) employing a DEM-based dynamic model with centripetal packing; approximately 6 by To and Stachurski (2004), using a spherical growth model, described as a concurrent method by Wouterse (2008); approximately 6 observed by Isola (2008), using drop and roll simulation, addition; and 6.14 as established by Silbert et al. (2002), via molecular dynamics, a concurrent method (Wouterse, 2008). It is important to highlight that the estimated limits for RCP align with the equation of state value, $\langle C \rangle = 6$, as suggested by Song et al. (2008), as well as the *parking number* $\langle Cp \rangle = 8.7$ put forth by Mansfield et al. (1996).

3.2. Order and the radial distribution function

Spheres arranged in lattice formations exhibit long-range, periodic order. The unit cells may be isotropic, as seen in simple cubic (SC), body-centered cubic (BCC), or face-centered cubic (FCC) structures, or they may display some degree of anisotropy, as in hexagonal close-packed (HCP) arrangements, despite the isotropic nature of the spheres themselves. The clusters that emerge in disordered materials are of significant interest, as they contribute to the characteristics of the resulting packing structure. Although the terms 'random loose packing' (RLP) and 'random close packing' (RCP) are often applied to disordered sphere arrangements, these structures exhibit discernible short-range order. This observation led Torquato et al. (2000) to advocate for the designation of maximally random jammed (MRJ) state when discussing such disordered systems. Both experimental findings and computational simulations have revealed radial distribution functions (RDF) for disordered spheres. One of the earliest RDFs demonstrating this order, which was modeled using a computer algorithm, was introduced by Matheson (1974), based on an experimental packing produced by Finney (1970). The RDF indicated a first peak at a diameter $\varnothing = 1$ for adjacent spheres, followed by two additional peaks, $\varnothing = \sqrt{3}$ and $\varnothing = 2$. These findings are illustrated in Fig. 2, adapted from (Isola, 2008), which depicts how the spherical shells surrounding the central shell correspond to the peaks observed in the RDF. Additionally, the observed peaks can be linked to distinct geometrical configurations. Specifically, for $\varnothing = \sqrt{3}$ this corresponds to a sphere positioned within a well created by two obstructing spheres. In the case of $\varnothing = 2$, the scenario involves an outer sphere being directly obstructed by an inner sphere that encircles the central sphere (see Fig. 2). Beyond $\varnothing = 2$ the radial distribution function (RDF) stabilizes, suggesting the absence of long-range order in the macroscopic arrangement. Aste et al. (2005) noted that the magnitude of the peaks increased with a rise in packing fraction; notably, the peak at $\varnothing = \sqrt{3}$ exhibited a more pronounced increase compared to the peak at $\varnothing = 2$ thereby affirming a growth in short-range order as packing fraction increased. The term 'steric factors' broadly encompasses this enhancement in order, attributed to heightened correlations among particles. The brown line depicted in Fig. 2 represents a step function, indicative of a packing arrangement devoid of order or correlation among particles and their interactions. Consequently, the RDF illustrated in Fig. 2 reflects a trend demonstrating a decline in order from random close packing (RCP, $\mu = 0$) thru random loose packing (RLP, $\mu = 50$) to an ideal packing scenario characterized by a lack of order or correlation, as represented by the step function (González García, 2015).

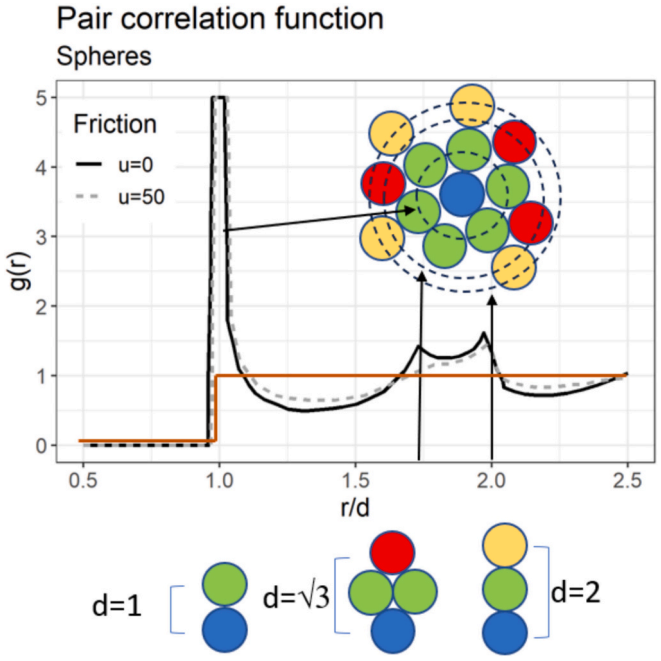

Fig. 2. Illustrates the pair correlation function for spheres arranged without friction ($\mu = 0$) and with a significant degree of friction ($\mu = 50$), as adapted from Yuan et al. (2021). The green spheres denote the initial layer of packing surrounding a central blue sphere. The red spheres indicate the configuration at a distance of $d = \sqrt{3}$, while the yellow spheres represent the arrangement at $d = 2$. The brown line depicts a step function characteristic of an uncorrelated system. (For interpretation of the references to colour in this figure legend, the reader is referred to the web version of this article.)

4. Packing of monosized grains of different shapes

4.1. Spheroids and spherocylinders

The exploration of shapes beyond spheres can naturally progress to the study of non-spherical particles such as spheroids and spherocylinders. Spheroids can be derived from a sphere by either elongating or compressing the z-axis, resulting in prolate spheroids, which resemble needles, or oblate spheroids, which take on a disk-like form. In contrast, the formation of a spherocylinder begins with a sphere that is bisected, followed by the gradual extension of a cylinder with an equivalent radius between the two hemispheres. This process initially yields a pill-shaped object, which transforms into elongated rods as the length of the cylinder increases significantly. These geometric forms are not only mathematically manageable but also serve as effective analogs for various environmental materials; for instance, oblate spheroids represent platy particles such as clays, while prolate spheroids and spherocylinders model fibrous materials, including roots, fungi, and peat fibers.

For a particle assembly to achieve stability, it is essential that the forces acting upon it are in equilibrium. In the context of cohesionless spheres, this necessitates a balance of contact forces. Conversely, non-spherical particles also experience torques, which also require balancing. Consequently, altering the shape of the particles introduces at least two significant new characteristics: the presence of torques and a variation in the number of degrees of freedom (df), alongside particle anisotropy, which can result in more complex packing arrangements compared to spherical particles alone. Spheres possess only three degrees of freedom, allowing movement along the x, y, and z axes. In contrast, spheroids ($a \neq b = c$) can rotate, providing them with five degrees of freedom, while general ellipsoids ($a \neq b \neq c$) exhibit six degrees of freedom. The phenomenon of jamming for spherical particles is solely dependent on translational jamming, whereas for aspherical particles, both translational and rotational jamming play a role. Bennett (1972) proposed that the RCP contact number should be 6, grounded in

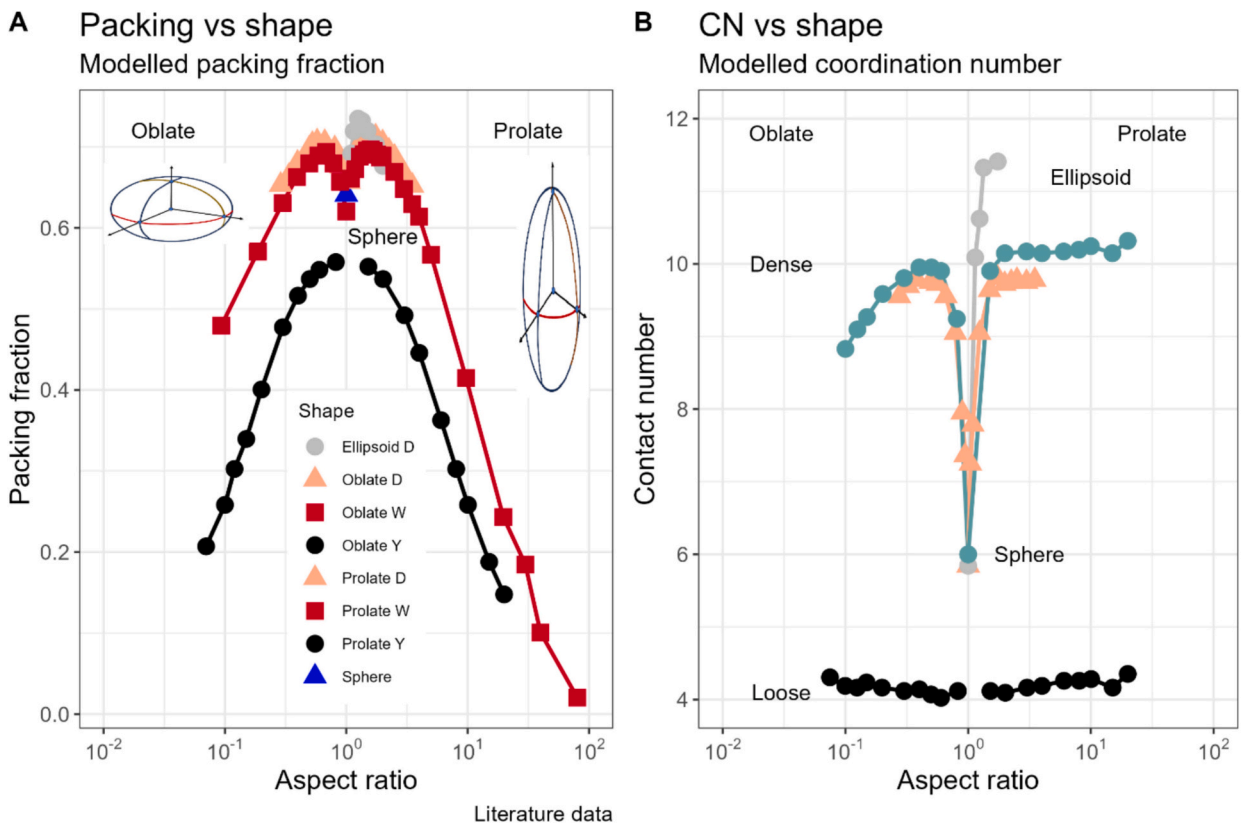

Fig. 3. A) The packing fraction and the average contact number ⟨C⟩ for models of oblate (left), prolate (right), and general ellipsoids are presented as a function of the aspect ratio. The digitized data for dense packings is sourced from Donev et al. (2004) (D); Wouterse et al. (2007) (W) while loose packing is from Yuan et al. (2021) (Y). B) The relationship between contact number and aspect ratio is illustrated for data from (Donev et al., 2004) and from (Yuan et al., 2021), distinguishing between loose packings (black solid circles) and dense packings (blue solid circles). (For interpretation of the references to colour in this figure legend, the reader is referred to the web version of this article.)

the principles of mechanical stability, leading to the conclusion that the average contact number can be expressed as ⟨C⟩ = 2df, a condition referred to as isostatic. The central thesis posits that a frictionless random packing must possess a sufficient number of constraints to adequately define the system. Donev (2006) demonstrated that packings composed of hard spheres are strictly isostatic, conforming to this principle. In contrast, aspherical particles exhibit hypostatic behavior, meaning their values fall short of the isostatic threshold, leading to a breakdown of the theory, as no discernible transition occurs from spherical to spheroidal shapes. Consequently, the average coordination number, ⟨C⟩, is established at 6 for an MRJ state of spheres. However, the isostatic values for spheroids (⟨C⟩ = 10) and highly anisotropic general ellipsoids (⟨C⟩ = 12) do not apply, as the hypostatic values are approximately 9.7 and 11.4, respectively, i.e. they fail to attain the isostatic benchmarks. Furthermore, as the aspect ratio of non-spherical particles increases, their shape characteristics become more pronounced. This indicates that the arrangements of these particles can exhibit not only periodic and short-range (glassy) orders but also orientational order (nematic). The level of anisotropy observed in these arrangements may significantly exceed that found in spherical particle packings, which has critical implications for the packing fraction. Such structural effects are commonly encountered in physical packings but can be overcome with computer simulation.

The previously established RCP limit for spherical particles was approximately 0.64. However, research conducted by Donev et al. (2004) revealed, through both experimental methods and simulation algorithms, that ellipsoidal particles could achieve higher packing densities, with RCP values ranging from approximately 0.68 to 0.71 (see Fig. 3a). This enhancement in packing density is attributed to the increased degrees of freedom associated with ellipsoids. The authors posited that '*to eliminate all local and collective degrees of freedom and ensure jamming, and forming more contacts, requires a denser packing of the particles*.' Their findings indicated that the optimal packing density was observed when the aspect ratio of the particles was around 1.5 for prolate shapes and approximately 0.67 for oblate shapes, resembling the form of an M&M candy. Their investigation illustrated how the packing fraction varied from that of spherical particles (~0.64) as the aspect ratio changed for both oblate and prolate particles. It is noteworthy that Donev's analysis was limited to specific aspect ratios. In contrast, Wouterse et al. (2007) endeavored to model the behavior of spheroids across a broader spectrum of aspect ratios (refer to Fig. 3a). Furthermore, Gan and Yu (2020) observed, based on the findings of Zhou et al. (2011), regarding poured packing, that oblate particles exhibited a lower packing fraction compared to prolate particles. However, both types of particles demonstrated an increase in packing density upon vibration, with prolate particles maintaining a packing fraction approximately 0.01 higher than that of oblate particles at their peak, corroborating the results of previous studies (Donev et al., 2004; Gan et al., 2016; Xu et al., 2022). This further emphasizes the significance of the method employed in generating a particle pack.

Donev's computational simulation revealed a significant increase in the number of contacts, rising from approximately 6 to around 10, resulting from a minor alteration in the aspect ratio of a particle transitioning from a spherical shape (Fig. 3b). Specifically, the aspect ratio was adjusted from 1 to 1.5 for prolate spheroids, while it decreased from 1 to 0.67 for oblate spheroids. Donev determined that a densely packed arrangement of spheroids exhibited an average contact number ⟨C⟩ of approximately 9.7, which is just below the threshold of 2df, where df equals 5, based on the degrees of freedom associated with isostatic packing (Fig. 3b). This increase in contact numbers is essential for

Table 2
The volumes (v), surface areas (s), radii of mean curvature (R), and exclusion fraction (V_{ex}/v) of a sphere and several non-spherical shapes. The radius of mean curvature and exclusion fraction correspond to randomly oriented convex particles. Adapted from Torquato and Jiao (2013).

Convex particle	v	s	$\overline{R}$	Exclusion fraction (V_{ex}/v)
Sphere Radius = a	$\frac{4\pi a^3}{3}$	$4\pi a^2$	a	8
Prolate spheroid Semiaxes a = c, b ≥ a e^2 = 1-(a/b)^2	$\frac{4\pi a^2 b}{3}$	$2\pi a^2\left(1+\frac{b}{ae}sin^{-1}e\right)$	$\frac{b}{2}\left(1+\frac{a^2}{b^2e}tanh^{-1}e\right)$	$2+\frac{3}{2}\left(1+\frac{b}{ae}sin^{-1}e\right)\times\left(1+\frac{a^2}{b^2e}tanh^{-1}e\right)$
Oblate spheroid Semiaxes a = c, b ≤ a e^2 = 1-(b/a)^2	$\frac{4\pi a^2 b}{3}$	$2\pi a^2\left(1+\frac{b^2}{a^2e}tanh^{-1}e\right)$	$\frac{b}{2}\left(1+\frac{a}{be}sin^{-1}e\right)$	$2+\frac{3}{2}\left(1+\frac{b^2}{a^2e}tanh^{-1}e\right)\times\left(1+\frac{a}{be}sin^{-1}e\right)$
Spherocylinder, radius a and cylindrical length h.	$\frac{\pi a^2(4a+3h)}{3}$	2πa(2a + h)	$\frac{h+4a}{4}$	$2+\frac{3(2a+h)(4a+h)}{a(4a+3h)}$

constraining the movement of anisotropic particles. Furthermore, aspherical ellipsoids demonstrated the capacity to achieve even higher packing densities of around 0.74, closely resembling the maximum density achievable by monosized spheres in face-centered cubic (FCC) or hexagonal close-packed (HCP) arrangements, with an average contact number of 11.4, again falling short of, but remaining consistent with, ⟨C⟩ = 2df, where df equals 6 for general ellipsoids. In a study conducted by Yuan et al. (2021) both dense and loose spheroid packings were examined; the dense packing exhibited contact numbers slightly exceeding 10, indicating a potential hyperstatic condition and mechanical over-determination. Neudecker et al. (2013) in their investigation of frictional tetrahedra, also found that the respective particle arrangements were hyperstatic, attributing this phenomenon to the packing methodology employed. Conversely, the loose packings analyzed by Yuan et al. (2021) revealed a contact number of approximately 4, categorizing them as hypostatic, even with an increase in aspect ratio (Fig. 3b). The plotted data in Fig. 3b exhibited a positive curvature, suggesting that contact numbers might approach 5 at an aspect ratio of around 100. This observation aligns with Donev's assertion (Donev, 2006) that a specific number of contacts is generally necessary to ensure the stability of aspherical particle arrangements. Donev et al. (2004) suggested that the quantity of contacts may remain near the level necessary to attain maximum density. Furthermore, they indicated that the subsequent reduction in density, as aspect ratios increase, is attributable to progressively stronger excluded volume effects (see Table 2, Fig. 6).

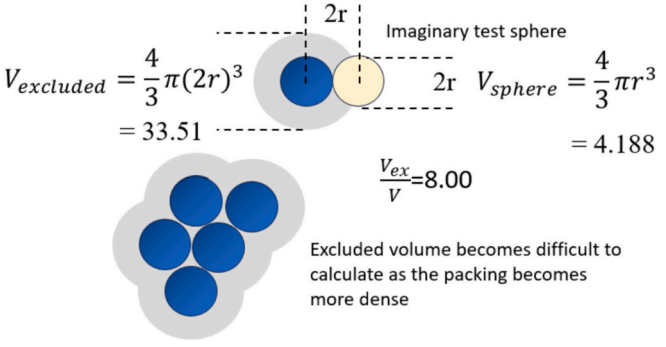

Fig. 4. Demonstration of the excluded volume effect, shown by an imaginary sphere (yellow) contacting a unit sphere (blue) at the top. The excluded volume 33.51 (grey) is greater than that of a unit sphere (blue) 4.188. The ratio of the excluded volume to the volume of the unit sphere V_{ex}/v is 8. (For interpretation of the references to colour in this figure legend, the reader is referred to the web version of this article.)

4.2. Particle exclusion volumes

Excluded volume (V_{ex}) refers to a physical concept that delineates the volume that remains inaccessible to the centers of other particles because of the presence of a primary particle. This concept is exemplified for a spherical particle, as depicted in Fig. 4.

The excluded volume of a spherical particle of radius (r) and volume (v) = (4/3)πr^3 is inaccessible to other test particles of radius r_1 or volume v_1 according to:

$$V_{ex} = \frac{4}{3}\pi(r+r_1)^3 = \left(v^{\frac{1}{3}} + v_1^{\frac{1}{3}}\right)^3 \quad (5)$$

When $r = r_1$, $V_{ex} = 8v$. The concept of exclusion volume has a significant historical background in the formulation of equations of state for fluids (Rusanov, 2010). This idea is integral to the van der Waals equation of state (Van der Waals, 1873) which serves as an extension of the ideal gas law, and is also present in Planck's equation of state (Planck, 1908). As illustrated in Fig. 4, the excluded volume (V_{ex}) associated with a single sphere of unit radius is calculated to be 33.51. When this value is normalized by the volume of the sphere (v), it yields what is known as the exclusion factor (f) (Rusanov, 2010).

$$f \equiv \frac{V_{ex}}{v} \quad (6)$$

As highlighted by Melnyk et al. (2022) the complexity of accurately determining the excluded volume escalates due to the necessity of accounting for the overlapping excluded volumes of multiple spheres, rendering the problem analytically intractable as the packing density increases.

This issue was explored in a series of publications concerning multicomponent packing (Rusanov, 2003a; Rusanov, 2003b; Rusanov, 2004; Rusanov, 2010). The authors demonstrated, utilizing excluded volume theory, how various approximations of the function f led to distinct and well-established equations of state for classical hard-sphere fluids. The volume parameters presented are average values for multicomponent systems as indicated in Eq. (6). The zero-order approximation for spheres yields a constant value of 8, which corresponds to the Planck equation of state for a monatomic gas. In contrast, the first-order approximation posits a linearly decreasing function with respect to the packing fraction (η), leading to the van der Waals eq. A second-order approximation produces a curve:

$$f^{(2)} = \frac{f_o - k_1\eta}{1+k_2\eta} \quad (7)$$

where f_o is the exclusion volume for the limiting value of a single sphere (8) and k_1 and k_2 are positive constants. The third-order approximation results in:

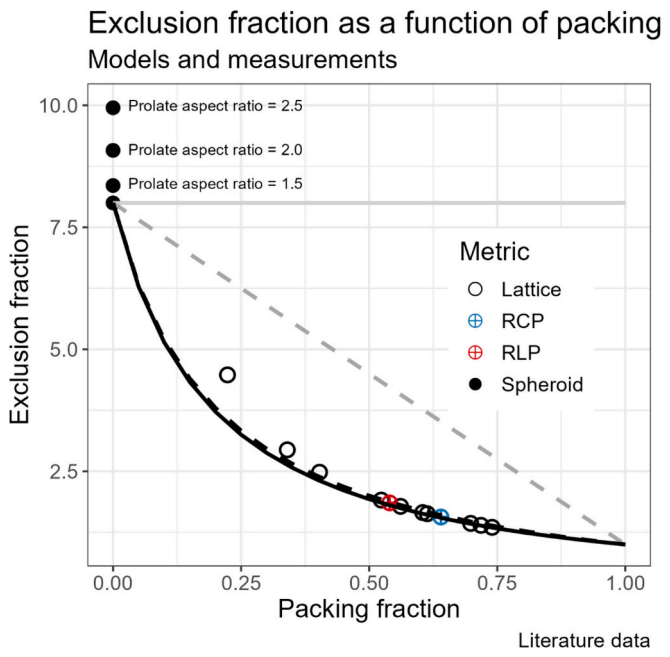

Fig. 5. The exclusion fraction for spherical particles according to Rusanov (2010) for different approximations based on excluded volume theory. The open circles stand for dense packings (lattices) where the exclusion fraction is assumed to be $1/\eta$, the crossed circles are $1/\eta$ for RCP and RLP. The assumption of $1/\eta$ for dense packing appears reasonable above $\eta = 0.5$ while diverging below 0.5. In the upper lefthand corner the exclusion fraction for prolate particles based on the equations in Table 2 is presented for low aspect ratios. The solid grey line is 8, equivalent to the zero-order approximation; the dashed grey line is first order; the dashed black line second and the solid black line third order (see Eqs. (7) and (8)).

$$f^{(3)} = \frac{f_o - k_1\eta + k_3\eta^2}{1 + k_2\eta} \tag{8}$$

Rusanov (2010) established the constants as follows: $k_1 = 3\,k^2$, $k_2 =$ 8-3 k, and $k_3 = k^3$ to determine the compressibility factor. In this context, k represents an unknown constant, which yields a simplified version of the Percus-Yevick approximation (Percus and Yevick, 1958; Reiss et al., 1959) when k is = 1. Consequently, in Eq. (8) if k = 1 then k_1 becomes 3, k_2, 5, and k_3, 1. Additionally, the empirical constants $k_1 = 2$ and $k_2 = 5$ are appropriate for the second-order approximation. The outcomes of the various approximations are illustrated in Fig. 5.

Rusanov (2010) introduced a derivation concerning clustered particles, where the volume of the cluster per particle, when divided by the volume of a sphere (denoted as v in the context of cluster volume or unit cell for lattices), is represented as f. In the scenario of a lattice structure such as face-centered cubic (FCC), this relationship corresponds to the ratio of the unit cell volume to the volume occupied by spheres within that unit cell. The calculation yields $Vc = 16\sqrt{2}r^3$ divided by $vt = 16/3\pi r^3$ resulting in $6/(\pi\sqrt{2}) \equiv f$. Consequently, by definition, $f \equiv 1/\eta$, resulting in FCC being approximately 1.35 and simple cubic (SC) being approximately 1.91. As illustrated in Fig. 5 the excluded volume derived from $1/\eta$ (Rusanov, 2010) shows a divergence from theoretical predictions at packing densities below approximately 0.5.

Melnyk et al. (2022) have recently revisited the topic concerning spheres, providing new insights into the complexities involved. They demonstrated that while calculating the excluded volume for a single sphere is straightforward, the task becomes increasingly challenging as additional spheres are introduced. The analytical evaluation of excluded volume becomes impractical due to the geometric complexities that arise. The authors identified that this difficulty stems from the positioning and overlapping of excluded volumes as the number of spheres increases. In densely packed arrangements, this leads to a heightened

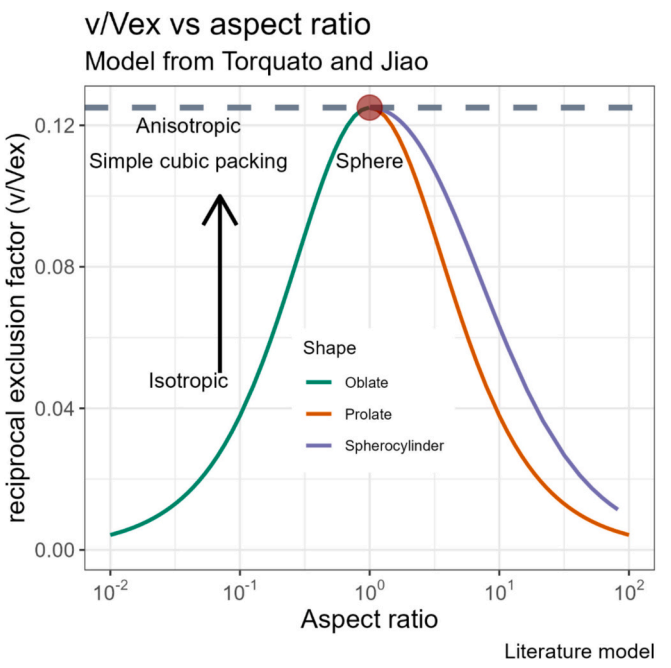

Fig. 6. The volume (v) over the excluded volume (V_{ex}) as a function of aspect ratio for oblate, prolate and spherocylindrical particles, calculated using the analytical solutions in Table 2 from (Torquato and Jiao, 2013). The curves are for randomly oriented isotropic packings, but the reciprocal of the exclusion factor increases if the particles become aligned as shown by the arrow. Aligned anisotropic particles in a dense simple cubic packing (dashed line) all have the same constant ratio ($v/V_{ex} = 0.125$).

level of correlation that must be accounted for in calculations, in contrast to dilute systems where such correlations are negligible; these correlations are integrated into the steric factor term.

A significant challenge lies in determining the excluded volume for shapes that are not spherical. In a notable advancement, Torquato and Jiao (2013) introduced a formula designed to compute the exclusion volume of a multi-dimensional hyper-particle with an arbitrary shape. This formula incorporates the d-dimensional volume, denoted as v, surface area, s, and radius of mean curvature $\overline{R}$ (or, equivalently, *mean width*). Subsequent developments for higher dimensions were presented by (Torquato and Jiao, 2022). For the case of d = 3 several important analytical formulas were established, enabling the calculation of exclusion volumes for various non-spherical geometries, such as oblate spheroids, prolate spheroids, and spherocylinders. The exclusion volumes (V_{ex}/v) relevant to d = 3 geometries utilized in this study are summarized in Table 2, which has been adapted from Table II in (Torquato and Jiao, 2013) providing solutions for a range of convex particle types.

The inverse exclusion volumes (v/V_{ex}) for the aforementioned shapes are illustrated in Fig. 6. This reciprocal representation is employed to bound the outcomes. As the aspect ratio deviates from the spherical values averaged across all orientations, V_{ex} experiences a significant and more rapid increase compared to v, leading to extraordinarily high values.

The circle depicted in Fig. 6 illustrates the value for a sphere, calculated as v/V_{ex} for a unit radius sphere, which equals 4.188/33.51 resulting in 0.125; conversely V_{ex}/v equals 8. The exclusion volumes for both prolate and oblate spheroids exhibit symmetry as per the corresponding equations presented in Table 2 and are also represented in Fig. 6. The dashed straight line traversing the sphere signifies a system of particles, whether oblate or prolate, that are aligned in a simple cubic packing. In such instances, the relationship $V_{ex}/v_{aligned}$ is expressed as 2^d. When the dimension is set to d = 3 this relationship yields $V_{ex}/v_{aligned} = 8$. As noted by Torquato (2012) this relationship remains

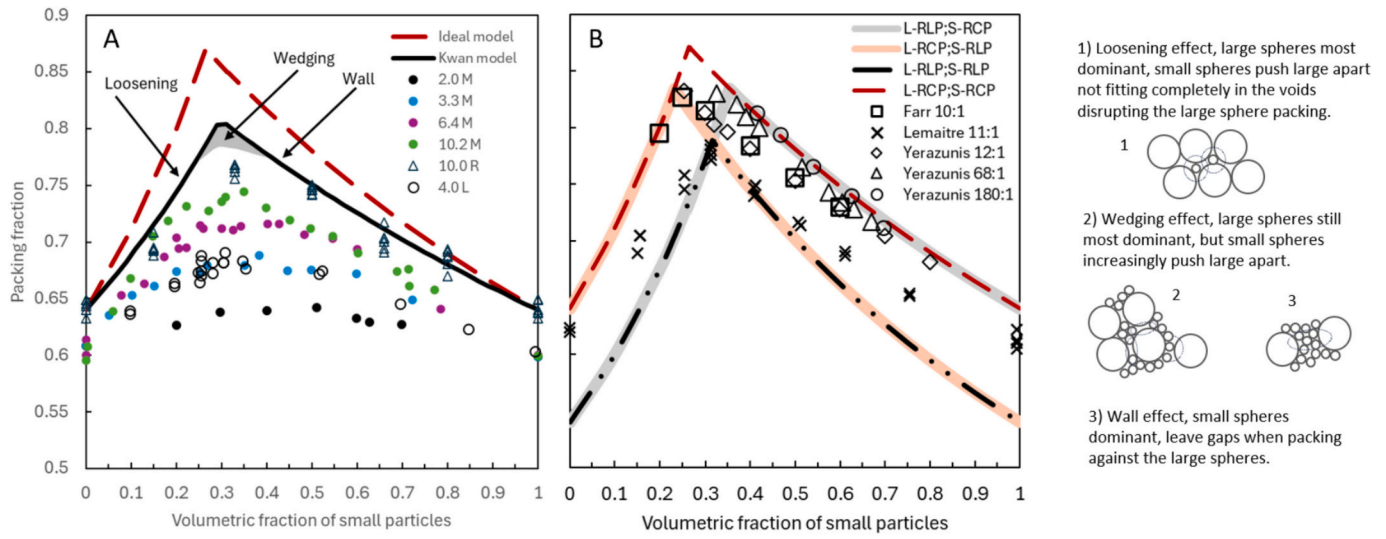

Fig. 7. a. Packing fraction of binary mixtures of spheres with data from (L,M & R, respectively) (Lemaitre et al., 1988; Mota et al., 2001; Robinson and Friedman, 2001) for a mixture of glass spheres with given size ratio. The solid black line represents the 2-parameter model of Kwan et al. (2013). The red dashed line the ideal packing model. 7b. RCP ($\eta = 0.64$) and RLP ($\eta = 0.54$) in different configurations of ideal packing forming the 4 different modes with the red dashed line representing the RCP upper bound and the black dashed line the RLP lower bound. Data for ideal packing is presented from (Farr and Groot, 2009; Lemaitre et al., 1988; Yerazunis et al., 1965). The text at the side shows the different packing effects described by Kwan et al. (2013). (For interpretation of the references to colour in this figure legend, the reader is referred to the web version of this article.)

consistent regardless of the shape of particles.

5. Particle size distribution and binary mixtures

Particle size distribution significantly influences the packing fraction of materials. The investigation of binary and multi-size mixtures is crucial and has been the focus of numerous studies (Brouwers, 2013; Dias et al., 2004; Furnas, 1931; Kwan et al., 2013; Lemaitre et al., 1988; Meng et al., 2014; Pinson et al., 1998; Sibellas et al., 2024; Sohn and Moreland, 1968; Visscher and Bolsterli, 1972; Yerazunis et al., 1965; Yu and Standish, 1988). Research indicates that the packing density of binary hard spheres is affected by particle size ratio, with smaller particles effectively occupying the voids between larger particles, leading to an increase in packing density (Mota et al., 2001). The optimal packing occurs when the voids created by larger particles are filled by smaller ones, this occurs when the volume of small spheres relative to the total volume is about one third and is known as ideal or theoretical packing (Furnas, 1931; Koltermann and Gorelick, 1995; Kwan et al., 2013).

Various models have been proposed to explain this phenomenon (Brouwers, 2013; Hopkins et al., 2011; Hopkins et al., 2012; Kwan et al., 2013; Mota et al., 2001; Visscher and Bolsterli, 1972). Furnas (1931) is recognized as the pioneer in addressing this issue, proposing a system characterized by 'ideal' behavior. The 'ideal' binary packing model is often used as a lower bound to the porosity of $\varphi_{min} = \varphi_{small} \times \varphi_{large}$ or an upper bound for its equivalent, the packing fraction of $\eta_{max} = (\eta_{small} + \eta_{large})\text{-}(\eta_{small} \times \eta_{large})$, which for RCP is $(0.64 + 0.64) - (0.64 \times 0.64) = 0.87$. However, empirical measurements revealed that actual materials generally fell short, even at high size ratios >15 (Dias et al., 2004). This led to the identification of several distinct phenomena associated with mixing that inhibited ideal behavior in real packings. One such phenomenon is the wall effect, which occurs when smaller particles encounter larger ones. The presence of larger particles disrupts the packing arrangement, potentially creating voids (see Fig. 7a). Another phenomenon, known as the loosening effect, arises when small particles interfere with the packing of larger particles, resulting in increased spacing between them (see Fig. 7a). Kwan et al. (2013) posited the necessity of considering a third phenomenon, termed the wedging effect, where a small particle is positioned between two larger particles, effectively prying them apart (see Fig. 7a). Collectively, these effects lead to a packing density that, at its peak, is usually lower than 0.78 for a size ratio of about 10:1, which is lower than the ideal packing limit of approximately 0.87, as well as the densest packing value of 0.825 proposed by (Hopkins et al., 2011; Hopkins et al., 2012), and to much lower peak densities for smaller size ratios (Fig. 7a).

Furthermore, four distinct types of ideal packing configurations are introduced, wherein either the large or small particles, or both, can be arranged in either a close-packed (RCP) or a loose-packed (RLP) manner (see Fig. 7b). The general form of the ideal packing model $\eta(f_s)$ for a binary mixture is $\eta = \eta_{Lmax} + [f_s/(1\text{-}f_s)]\ \eta_{Lmax}$ (η - packing fraction of the mixture, η_{Lmax} – maximum possible packing fraction of the large particles) for the volumetric fraction of small particles in the range of $f_s = 0$ to f_{smax} (f_{smax} - f_s that yields the peak η, η_{max}, left wings, Fig. 7b), and for $f_s = f_{smax}$ to 1 (right wings, Fig. 7b) it is $\eta = 1/[1 + (1/\eta_{Smax} - 1)f_s]$ (η_{Smax} – maximum possible packing fraction of the small particles). The range of peak packing densities (η_{max}) corresponding to the 4 ideal packing modes is 0.789 to 0.870, achieved at a wider range of volumetric fraction of small particles (f_{smax}) of 0.233 to 0.353 (Fig. 7b). The notable differences in η_{max} and especially f_{smax} values, if compared to those obtained in experimental and computational simulations, may suggest which type of packing—large or small particles—is more disrupted within the mixture. Consequently, this analysis can provide insights into which of the identified disturbance mechanisms (Fig. 7, Dias et al., 2004; Kwan et al., 2013) is more prevalent: the "loosening and wedging effects" impacting the packing of larger particles or the "wall effect" influencing the packing of smaller particles.

The data from Yerazunis et al. (1965) for mixtures of size ratios of 12, 67.7 and 180 show clearly the convergence of the mixture packing density with the ideal large-close-or-loose-small-close packing mode for $f_s > f_{smax}$ at "infinite" size ratio (Fig. 7b). Notably, in the case of binary mixtures with a size ratio around 10, such as the dataset from Lemaitre et al. (1988) for a size ratio of 11 (Fig. 7b) and that of Farr and Groot (2009) for a size ratio of 10 (Fig. 7b), the two end members of either large or small particles (away from f_{smax}) are being packed closer to an RCP mode; but close to their peak mixture density of η_{max} at f_{smax}, their ideal packing mixture is more likely comprised of two RLP packing domains of the large and small particles (Fig. 7b). The packing configuration varies continuously from approximately close-close to approximately loose-loose upon mixing.

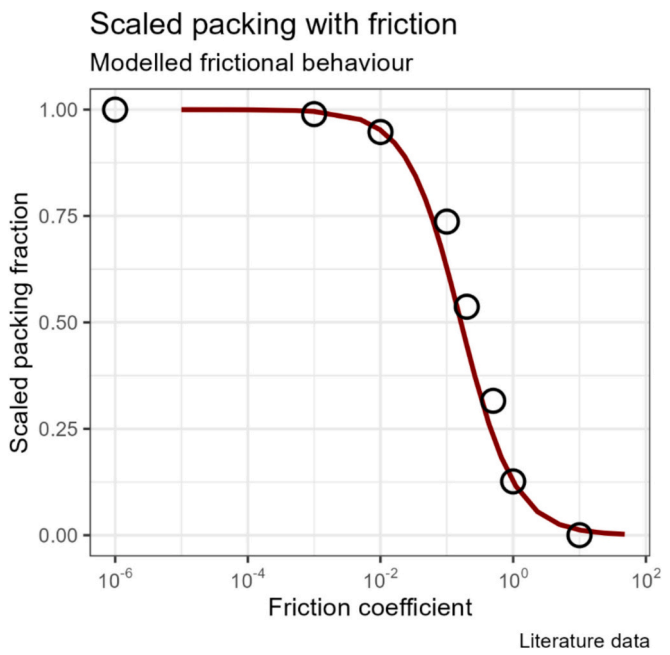

Fig. 8. The scaled packing fraction for monosized particles (η(μ), 0–1) as a function of the coefficient of static friction (μ), shown on a log scale with the data of Silbert (2010) (black circles) and the empirical model from Yuan et al. (2021) as the dark red line. (For interpretation of the references to colour in this figure legend, the reader is referred to the web version of this article.)

6. Inter-particle forces

6.1. Cohesionless particle packings > ~100 μm

Granular packings are characterized by their cohesionless and free-flowing nature, which establishes a lower size threshold of approximately 100 μm for such materials. Below this threshold, cohesive forces become increasingly significant in influencing the packing structure. In contrast, for particles larger than 100 μm, gravitational forces prevail, with the coefficient of friction (μ) and the coefficient of restitution (e) exerting opposing influences on the configuration of a poured packing (Wang et al., 2021). The coefficient of friction is defined as the ratio of the frictional force between two surfaces to the normal force acting upon them, whereas the coefficient of restitution, which quantifies energy loss, is defined as the ratio of the relative velocity of separation post-collision to the relative velocity of approach prior to collision. In their study on poured packings that form granular beds, Wang et al. (2021) observed that as the coefficient of friction increased from 0.1 to 0.9, the density of the packing decreased from approximately 0.535 to 0.485, and the average coordination number (⟨C⟩) diminished from 5.46 to 4.63. Conversely, an increase in the coefficient of restitution from 0.1 to 0.9 resulted in a density rise from about 0.515 to 0.545, alongside an increase in ⟨C⟩ from 5.18 to 5.36.

The presence of friction in granular materials influences the packing fraction, transitioning between the RCP and RLP states (Silbert, 2010; Yuan et al., 2021). Silbert (2010) illustrated this relationship, which is further depicted in Fig. 8. Subsequently, Yuan et al. (2021) confirmed that this relationship is applicable to various particle shapes, revealing that when the data is normalized, it aligns onto a single curve. The empirical equation that characterizes this relationship is as follows:

$$\eta(\mu) = \frac{1}{1 + (\mu/\mu^*)^{\alpha}} \tag{9}$$

where η(μ) is the normalized packing fraction for the friction coefficient, μ is the coefficient of static friction, μ^* is 0.1636 and the exponent α is 1.07 (Fig. 8). The coefficient of static friction for environmental materials likely sits between 0.1 and 1; for example, quartz-dominated sandstone was found to lie between ~0.1–0.2 (Senetakis et al., 2013). This shows packing of sand is likely to be mid-range between RCP and RLP (Fig. 8). Friction values will increase towards ~1 depending on the material and its surface properties.

6.2. Cohesive particle packings < ~100 μm

As particles decrease in size, cohesive forces increasingly influence the arrangement and structure of the particles (Gan et al., 2016). A series of studies conducted by Yang et al. focused on the packing behavior of particles smaller than 100 μm (An et al., 2008; Yang et al., 2007; Yang et al., 2000; Yang et al., 2003). Notably, the initial study in this series integrated the van der Waals (vdW) force into the analysis of cohesionless granular materials larger than 100 μm to simulate packing behavior. The researchers distinguished between surface forces, such as rolling and sliding friction, and body forces, determined by the Hamaker constant and particle density. Their findings indicated that the packing fraction diminished as the coefficients of sliding and rolling friction and the Hamaker constant decreased. Conversely, an increase in particle density was associated with a higher packing fraction for larger particles. Essentially, the interplay of friction and the vdW force, represented by the Hamaker constant, enhances the 'stickiness' of the particles. As particle size diminishes, the influence of gravity wanes, and this 'stickiness' contributes to a looser particle arrangement. Furthermore, Yang et al. (2000) demonstrated that porosity increased with a rising force ratio χ = vdW/gravity (mg), with vdW forces beginning to significantly affect porosity at χ values exceeding approximately 10^2. Other cohesive forces that may be relevant, particularly in the context of packing of hydrophilic soil particles, include capillary bridging forces in the presence of water, which function similarly to the attractive vdW forces; however, vdW forces generally become negligible until particle sizes reach approximately 1 μm (clay sized) or less, as noted by(Li, 2005).

Yang et al. (2000); (Yang et al., 2003) presented an empirical function linking the macroscopic packing fraction (η) to the microscopic structure described by ⟨C⟩.

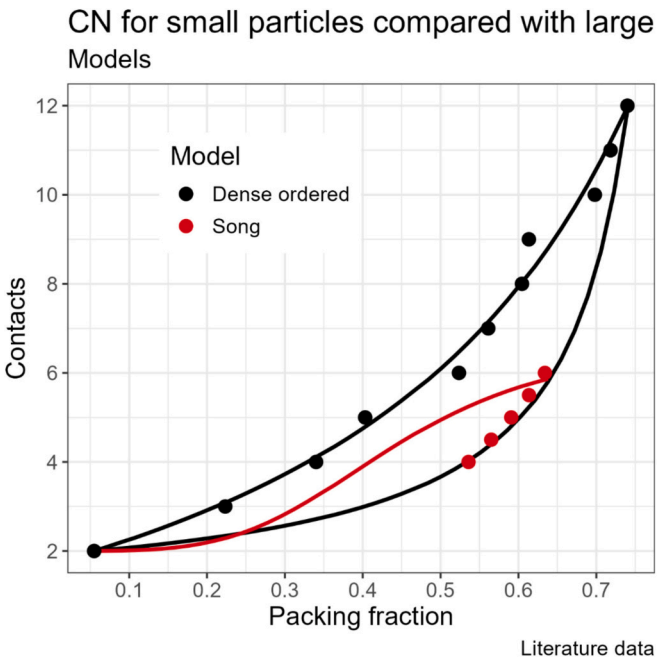

Fig. 9. The model of Yang et al. (2000) Eq. (10) redline, compared with the black lines highlighting the approximate bounds Eq. (3) and the data for dense ordered packings (Cumberland and Crawford, 1987) and the model output of (Song et al., 2008) Eq. (2).

$$\langle C\rangle = \langle C_0\rangle \frac{1+m(\eta)^4}{1+n(\eta)^4} \tag{10}$$

C_0 is the minimum number of contacts, considered to be 2, forming chains and consistent with Gardner (1966); $m = 87.38$ and $n = 25.81$ are constants. The function is drawn in Fig. 9 (red line) and falls within the approximate bounds proposed earlier in Eq. (3). It contrasts to the change in ⟨C⟩ path followed for particles greater than 100 μm and captured by Song's equation of state Eq. (2) shown by the red solid spheres.

Electrostatic forces play a significant role in soils, particularly in relation to clay particles. Clays may exhibit a neutral charge or possess a net charge, which is more commonly observed. These clays can develop a range of structural hierarchies, from individual platelets to tactoids and aggregates, influenced by the ionic strength and composition of the soil solution (Dor et al., 2020). Notably, high porosity in clays is evident irrespective of whether the particles are charge neutral or carry a net charge. The interplay of cohesive, adhesive, and repulsive electrostatic forces is contingent upon the specific characteristics of the clay (Rotenberg et al., 2011). For example, talc, which is charge neutral, still achieves a high porosity (~0.75) primarily through cohesive forces, followed by adhesion as it undergoes hydration (González-Teruel et al., 2020; Rotenberg et al., 2011). In the context of environmental materials like soils, the surface charge is balanced by counterions, some of which are adsorbed onto the surface. Consequently, in the packing of fine materials, cohesive forces tend to prevail over gravitational forces.

7. Modeling the packing of granular media

Numerous simulation techniques addressing the primary packing observables (η and ⟨C⟩) are documented in the literature, as summarized by (Donev, 2006; Isola, 2008; Wouterse, 2008). One such technique is Random Sequential Addition (RSA), which involves the random placement of particles into a pre-existing arrangement of fixed particles, ensuring no overlaps (Widom, 1966). Wouterse (2008) noted that, '*a major disadvantage of this method is that as the number of spheres increases it becomes increasingly hard to add additional spheres. Furthermore, the volume fraction is too low for spheres to be jammed.*' Consequently, if the condition of particle contact is not enforced, the simulation will yield a packing fraction considerably lower than the RCP threshold (González García, 2015; Sherwood, 1997). Additionally, Wouterse (2008) identifies concurrent methods, which involve the initial presence of all particles, including techniques such as Molecular Dynamics, Overlap Elimination, Energy Minimization, and Contact-Network Based methods. Furthermore, Williams and Philipse (2003) introduced an alternative approach known as the Mechanical Contraction Method (MCM).

7.1. Modeling of the packing fraction of uncorrelated monosized particles

The development of empirical models that accurately reflect the fundamental physical properties of particle packing is essential for investigating environmental materials. The characteristics outlined previously highlight the significance of various factors, including contact number, excluded volume, correlation, steric effects, particle size distribution, and particle anisotropy, which are crucial components in formulating an effective empirical model. Additionally, interaction effects will be addressed subsequently.

Philipse (1996) conducted a study on the arrangement of spherocylinders and introduced a model for random contacts. This model established a relationship between the average contact number, ⟨C⟩, the particle number density, and the excluded volume, drawing upon the methodology proposed by Onsager (1949) for V_{ex}. The findings can be expressed as an ideal packing equation applicable to uncorrelated contacts (Jia et al., 2019; Philipse, 1996; Wouterse et al., 2009; Wouterse et al., 2007):

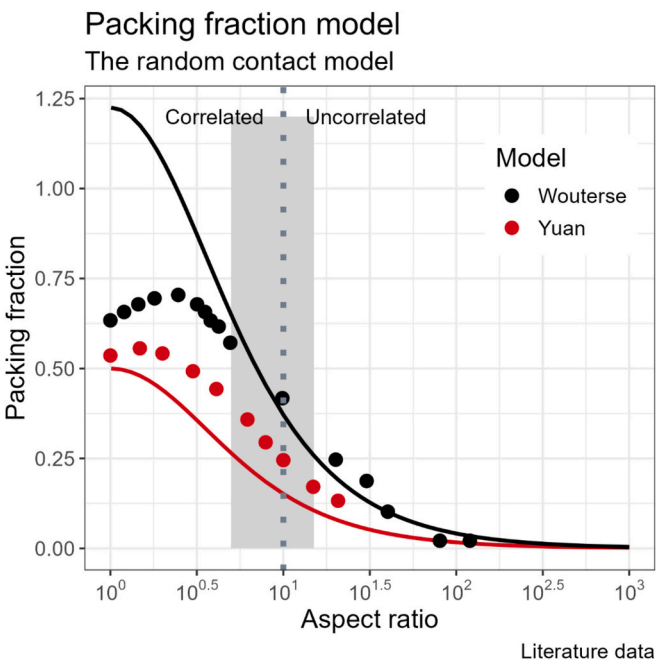

Fig. 10. Packing fraction of spherocylinders modeled using the random contact model (Philipse, 1996) (lines) and compared with the simulations of Wouterse et al. (2007) for dense packing and Yuan et al. (2021) for loose packing. Based on the modeling the radial distribution function illustrated in Fig. 2 reaches a step function between AR = 5–15 (González García, 2015) shown by the grey box. The grey dotted line is consisted with the radial distribution function corresponding to an aspect ratio of 10 in (González García, 2015). Both (Philipse, 1996) and (González García, 2015) considered an aspect ratio of L/D ≈ 15 is that transition between correlated and uncorrelated contacts.

$$\eta = \langle C\rangle \frac{v}{V_{ex}} \tag{11}$$

The variable v represents the volume of the particle under consideration; the excluded volume is denoted as V_{ex}, which can be calculated for various particle geometries as outlined in Table 2. Philipse (1996) noted that this model is applicable solely to dilute particle concentrations, allowing for the neglect of correlation factors. In his study, Philipse (1996) reported an average value of 10.8 ± 0.4 for the parameter ⟨C⟩, while (Williams and Philipse, 2003) documented a value of 10.2, and Wouterse et al. (2009) provided an experimental value of 9.8, which aligns with the modeling results presented by Donev (2006) in Fig. 3b. Eq. (11) also using the expression for the exclusion volume-dependence on the aspect ratio of prolate particles (Fig. 6) is illustrated for both loose (⟨C⟩ = 4) and dense (⟨C⟩ = 9.8) configurations, and these results are compared with the models proposed by Wouterse et al. (2007), and Yuan et al. (2021) in Fig. (10). The dense packing scenario demonstrates a reasonable correlation for aspect ratios exceeding approximately 10, as indicated by the dotted line in Fig. 10 consistent with the radial distribution function in Fig. 2.14 in González García (2015). This observation is consistent with the RDF exhibiting a step-like behavior, with the transition zone emphasized by the grey box, as modeled by González García (2015). Philipse (1996) (Fig. 4 in their article) indicated the transition between increasing numbers of multi-contact correlation (correlated) and uncorrelated lying around Length/Diameter (L/D) of 15. In contrast, for loose packing, the random contact model (red line in Fig. 10) consistently yields results below the output of Yuan et al. (2021) (red circles). Nevertheless, it appears to be trending towards convergence at aspect ratios around 100 or slightly lower. The correlation of contacts in packed, e.g. prolate particles, depends on their aspect ratio. When the aspect ratio is low (particle shape close to spheres), the particles tend to pack in a more ordered manner fitting

Table 3
The determined constants C_1 and C_2 using Eq. (13) for the ordered packings, the RCP and RLP and the constants determined by fitting RLP to a value of $\langle C \rangle = 5$ and RCP to a value of $\langle C \rangle = 10$ with only C_2 being adjusted but not multiplied by $\langle C \rangle$.

Packing fraction (η)	Contact number ⟨C⟩	Contact term	(C_1)	Steric term	(C_2)
0.055	2	1.079 × ⟨C⟩	2.16	6.870 × ⟨C⟩	13.7
0.2234	3	1.355 × ⟨C⟩	4.065	6.078 × ⟨C⟩	18.23
0.3401	4	1.418 × ⟨C⟩	5.672	5.899 × ⟨C⟩	23.60
0.4031	5	1.392 × ⟨C⟩	6.960	5.974 × ⟨C⟩	29.87
0.5236	6	1.431 × ⟨C⟩	8.586	5.861 × ⟨C⟩	35.17
0.5612	7	1.389 × ⟨C⟩	9.723	5.982 × ⟨C⟩	41.87
0.6045	8	1.362 × ⟨C⟩	10.90	6.059 × ⟨C⟩	48.47
0.6134	9	1.318 × ⟨C⟩	11.86	6.184 × ⟨C⟩	55.66
0.6981	10	1.328 × ⟨C⟩	13.28	6.156 × ⟨C⟩	61.56
0.7183	11	1.301 × ⟨C⟩	14.31	6.232 × ⟨C⟩	68.55
0.7405	12	1.247 × ⟨C⟩	14.96	6.027 × ⟨C⟩	72.32
0.536	RLP (4)	1.706 × ⟨C-sphere⟩	6.82	5.072 × ⟨C⟩	20.3
0.634	RCP (6)	1.539 × ⟨C-sphere⟩	9.23	5.551 × ⟨C⟩	33.3
0.536	RLP-fitted to data	1.392 × ⟨5⟩	6.96		21.1
0.634	RCP-fitted to data	1.328 × ⟨10⟩	13.3		65.4

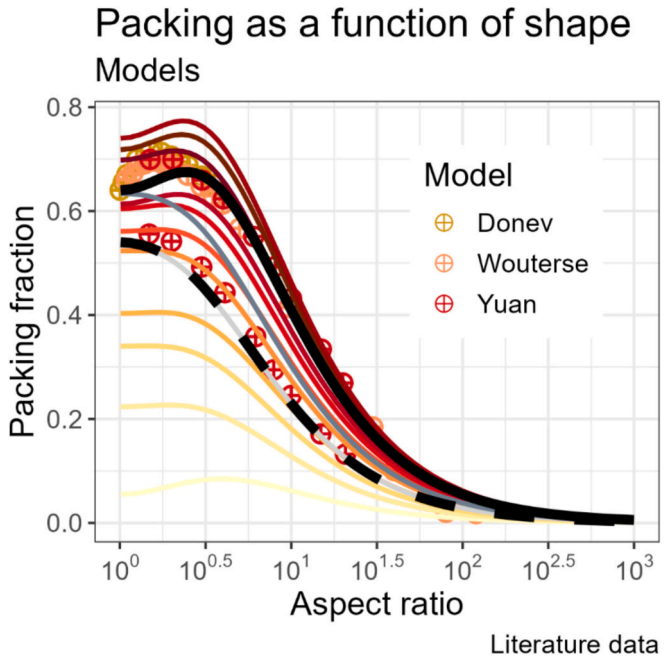

Fig. 11. The response curves for $\langle C \rangle = 12$ (top brown line) to $\langle C \rangle = 2$ (bottom yellow line) in descending order with an interval of 1. The dark grey line is RCP and the light grey line is RLP. The thick solid black line is (RCP-fitted) and the thick dashed black line is (RLP-fitted). The markers are for the models of the respective authors. (For interpretation of the references to colour in this figure legend, the reader is referred to the web version of this article.)

together more efficiently and forming structured arrangements. As a result, the contacts between particles are correlated, meaning the position and orientation of one particle influences the neighboring particles. On the contrary, high aspect ratio prolates tend to pack in a more disordered manner, and the contacts between particles are uncorrelated, meaning the position and orientation of one particle does not significantly influence the neighboring particles.

7.2. Modeling of the packing fraction of correlated monosized particles

Yuan et al. (2021) proposed an empirical equation for non-spherical particles with loose packing to take account of particle steric factors (correlation).

$$\eta = C_1\left(\frac{v}{V_{ex}}\right) - C_2\left(\frac{v}{V_{ex}}\right)^2 \tag{12}$$

where C_1 is an empirical parameter that should be related to the average contact number across particle shapes ⟨C⟩ as per (Philipse, 1996) and C_2 is an empirical constant related to correcting higher-order steric interactions (correlation) between particles; the constants are assumed to be independent of aspect ratio (on which the contact number is only weakly dependent, Fig. 3). One might assume that both C_1 and C_2 are related to the contact number and hence Eq. (12) becomes:

$$\eta = C_1(\langle C \rangle)\left(\frac{v}{V_{ex}}\right) - C_2(\langle C \rangle)\left(\frac{v}{V_{ex}}\right)^2 \tag{13}$$

Adjusting the packing fractions to align with those observed in the most efficiently packed monosized spheres, as well as the RCP and RLP configurations (refer to Table 3), and calculating (v/V_{ex}) corresponding to the specific aspect ratios of prolate particles (see Table 2), enables the determination of the constants C_1 and C_2. The resulting response curves are illustrated in Fig. 11, accompanied by simulated packing representations (denoted by crossed circles) (Donev et al., 2004; Wouterse et al., 2007; Yuan et al., 2021).

The colored lines represent the responses for packings ranging from the densest (0.74) to the least dense (0.055) as detailed in Table 3. The constants, $C_1/\langle C \rangle$ and $C_2/\langle C \rangle$, exhibited consistency, with a mean value for ordered packings, although (Yuan et al., 2021) were not addressing ordered packing, with ⟨C⟩ falling within the range of 3 to 12, where $C_1 \sim 1.35 \times \langle C \rangle$ and $C_2 \sim 6.05 \times \langle C \rangle$ (refer to Table 3); It is important to note that the model is sensitive to these parameters. A similar methodology was employed to determine the responses by first, fixing the contact numbers to those of spheres, which is not appropriate for non-spheres, so for RLP (⟨C-spheres⟩ = 4) and RCP (⟨C-spheres⟩ = 6), the responses are represented by dark grey (RCP) and light grey (RLP) solid lines, respectively. The RCP model tends to underestimate the packing response, at low aspect ratios while the RLP model also underestimates the response, albeit it aligns more closely with the simulation results presented by (Yuan et al., 2021). This likely occurs because the contact values for spheres are under representative for non-spheres and ⟨C⟩ represents some form of average number for all shapes, not just spheres.

The analysis of the response curves RCP ($C_1 = 1.539 \times \langle 6 \rangle$) and RLP ($C_1 = 1.706 \times \langle 4 \rangle$) reveals a consistency with RCP-fitted ($C_1 = 1.328 \times \langle 10 \rangle$) and RLP-fitted ($C_1 = 1.392 \times \langle 5 \rangle$) (which required the average contact numbers of 4 and 6 to be adjusted to 5 and 10 for the model to be compatible with the data, which makes sense given the majority of non-spherical particles) as the aspect ratio exceeds 10, indicating a lack of correlation. To achieve an empirical fit, C_1 was assigned these values corresponding to the respective packing, while C_2 was modified with the packing fraction aligned to RCP and RLP (as shown in Table 3 for RLP-fitted and RCP-fitted). This adjustment produced the response curves illustrated in Fig. 11, with the RCP-fitted model represented by a solid black line and the RLP-fitted by a dashed black line. One could contend, as suggested by Yuan et al. (2021) that C_1 ought to represent an average value of ⟨C⟩, which aligns reasonably with the contact values derived

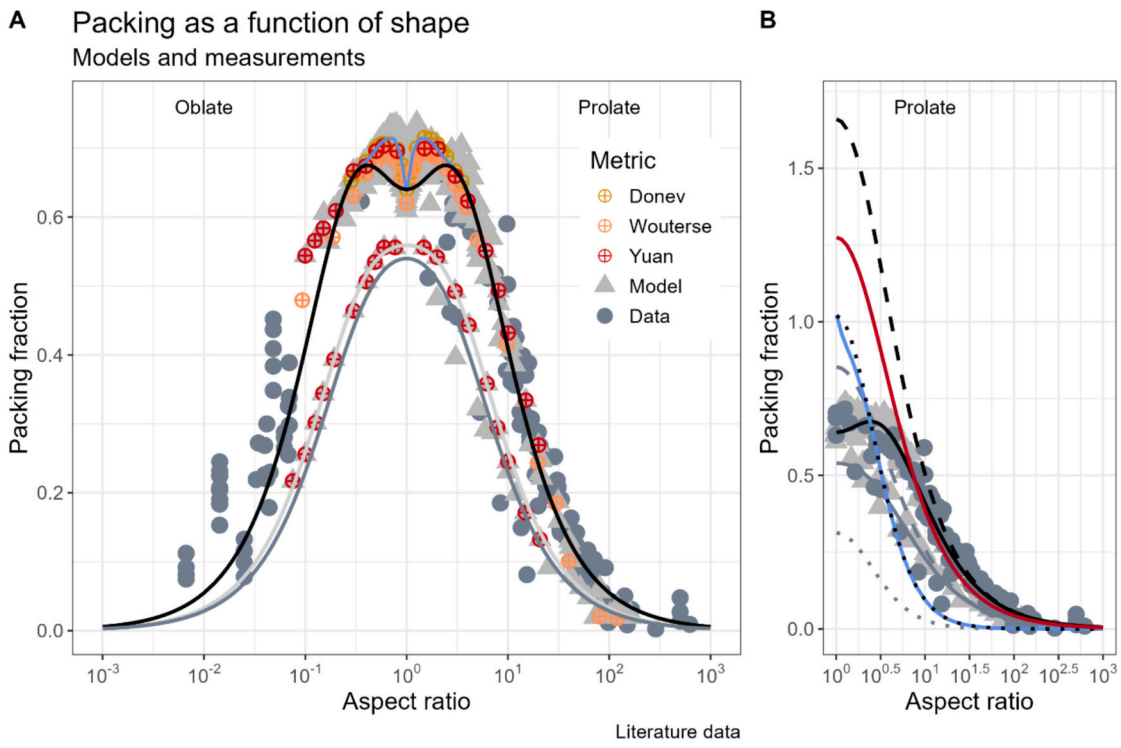

Fig. 12. A) Empirical measurements for spheroids (solid circles) (oblate clay-like particles and prolate fiber-like particles) and model simulations (triangles) with selected model simulations highlighted from (Donev et al., 2004); (Wouterse et al., 2007) and (Yuan et al., 2021). The three lines represent Eq. (12) with values for constants $C_1 = 7.868$ and $C_2 = 27.157$, thin pale grey line corresponding to (Yuan et al., 2021); (RLP-fitted, $C_1 = 6.82$ and $C_2 = 20.3$) the dark grey line; and (RCP-fitted, $C_1 = 13.3$ and $C_2 = 65.4$) the solid black line, Eq. (13) and Table 3 (constants from fitting model by minimizing SSE with data). The blue line is Eq. (14) with a modified steric contribution to model the dense packing. B) The red line is the average contact model for the dense packing of Philipse (1996) applied by Williams and Philipse (2003) with $\langle C \rangle$ =10.2 for dilute spherocylinders Eq. (11). The solid lines are RLP-fitted, dark grey; and RCP-fitted, black. The dashed lines are the contributions of the respective contact term, and the dotted lines are the steric term. The blue line is the contributions of the modified steric term to account for dense packing. (For interpretation of the references to colour in this figure legend, the reader is referred to the web version of this article.)

from simulation (refer to Fig. 3b); however, employing a multiplier yields a superior fit. Therefore, it is prudent to regard this model as an empirical approximation that effectively encapsulates certain physical responses associated with contact and steric effects.

Results for oblate and prolate particles are illustrated in Fig. 12a, which includes a compilation of empirical data represented by dark grey circles and computer simulations indicated by pale grey triangles. Notable model outcomes are marked in light brown (Donev et al., 2004); orange, (Wouterse et al., 2007), and red (Yuan et al., 2021). Furthermore, Eq. (12) is depicted with constants $C_1 = 7.868$ and $C_2 = 27.157$ as a pale grey line (Yuan et al., 2021). The RLP-fitted results are shown as a dark grey line, while the RCP-fitted results are represented by a black line, constants were determined by fitting the model to the data for aspect ratio's greater than about 10. The RCP-fitted line continues to exhibit certain characteristics of the response; however, it lacks the distinctive bump observed at low aspect ratios (0.5–2), as previously noted by Donev et al. (2004) and others for particles that deviate from a spherical shape (aspect ratio < 1 or > 1). The equation (black line) serves as a valuable representation of the empirical data, effectively capturing nearly all responses except for the most pronounced ones within the aspect ratio range of 0.5–2. To accurately represent the dense packing response for aspect ratios between 0.5 and 2.0, an additional empirical function (Jacquelin, 2024) is introduced in Eq. (14), depicted as the blue line in Fig. 12a, which modifies the steric contribution. The constant L, set to 0.07, determines the height of this function, resulting in a maximum porosity of 0.71 when combined with Eq. (12), aligning with the findings of Donev et al. (2004).

$$\eta = C_1\left(\frac{v}{V_{ex}}\right) - \left\{\left[C_2\left(\frac{v}{V_{ex}}\right)^2\right] - \left[\frac{L}{1 + be^{-k(AR)} + ce^{h(AR)}}\right]\right\} \quad (14)$$

$C_1 = 13.3$.
$C_2 = 65.4$.
L = 7.0E-02.
b = 3.582E+28.
k = 5.778E+01.
c = 6.335E-04.
h = 3.939E+00.

AR is the aspect ratio, related to (v/V_{ex}) by the equation for spheroids in Table 2.

Fig. 12 b disaggregates the model into its constituent elements. The solid lines represent the RLP-fitted (depicted in grey) and RCP-fitted (illustrated in black) models. The long dashed lines correspond to the contribution from the contact term, which is the first term in Eq. (13) for both RLP (grey) and RCP (black). In contrast, the dotted lines indicate the steric contribution, represented by the second term in Eq. (13) for RLP (grey) and RCP (black). The blue line illustrates the model including the modified steric contribution with the addition of the third term in Eq. (14). This modification is introduced to highlight that, to accurately reflect the response of dense packing for aspect ratios less than 2, the second steric term in Eq. (12) must be dampened, as indicated in Eq. (14). The solid red line represents the average contact model proposed by Philipse (1996) (Eq. (11)), as applied by Williams and Philipse (2003) with an average contact value $\langle C \rangle$ of 10.2 for dilute spherocylinders. As anticipated, this model does not align with the data until an aspect ratio of approximately 10 is attained; beyond this threshold, it accurately describes the data, underscoring the significance of excluded volume effects in characterizing the packing of increasingly anisotropic particles, even when the excluded volume is assessed for non-interacting particles. This empirical model (Eq. (14)) serves as a valuable tool for investigating the general behavior of environmental materials.

7.3. Modeling of the packing fraction of binary and multi-size particle mixtures

The initial focus on modeling monosized hard spheres naturally leads to an examination of how the introduction of shape influences particle interactions. Subsequently, it is essential to investigate the effects of varying particle size ratios on packing arrangements. This inquiry can be framed within the context of binary, ternary, or multi-size particle mixtures, which are prevalent in natural materials, particularly in soils. As outlined in the previous section, variations in particle size ratios will impact excluded volume, contact numbers, and steric factors as taken into account in Eq. (13). Utilizing existing literature, one can assess the probable effects of binary and multi-size mixtures on packing configurations through the application of Eq. (13). To effectively employ this equation, it is necessary to determine how these mixtures are expected to modify excluded volume, contact numbers, and steric interactions.

The excluded volume for binary mixtures of hard spheres was proposed by de Lange Kristiansen et al. (2005):

$$\frac{1}{8}\frac{\langle V_{ex}\rangle}{\langle V_p\rangle} = \frac{f^2 + (1-f)^2\gamma^3 + \frac{1}{4}f(1-f)(1+\gamma)^3}{f + (1-f)\gamma^3} \tag{15}$$

The term $\langle V_{ex}\rangle$ represents the statistically averaged excluded volume for the binary mixture; where V_p denotes the volume of a sphere; f indicates the number fraction of small spheres, and γ signifies the size ratio, (large/small). The findings indicate that the average excluded volume deviates from the value of 8, exhibiting a decline as the proportion of small spheres in the mixture with large spheres increases. A larger size ratio results in the formation of a trough, with minimum values of 4 and 3 being attained. This observation aligns with the physical understanding that the excluded volume diminishes as smaller spheres occupy the spaces between larger ones.

Contact numbers are not easily accessible and vary based on the classification of particles, whether they are large or small, and their respective combinations. These variations lead to what are known as partial coordination numbers. The overall mean contact number, denoted as ⟨C⟩, can be derived from these partial means. In a study conducted by Pinson et al. (1998) it was demonstrated that the overall mean (⟨C⟩ ~ 6) aligns closely with the monosized mean for random close packing (RCP), which is also ⟨C⟩ = 6, despite significant variations in the partial means; this finding was corroborated by Sibellas et al. (2024). Additionally, computer simulations utilizing mechanical contraction (de Lange Kristiansen et al., 2005) revealed that the mean contact number

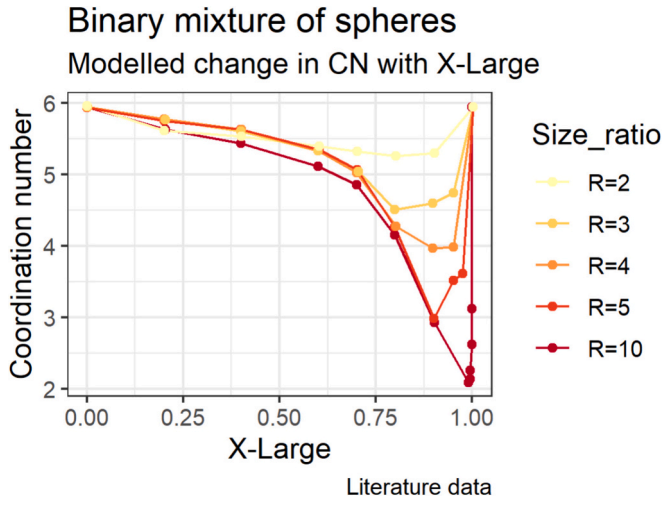

Fig. 13. The change in contacts ⟨C⟩ as large spheres are mixed in small for a range of size ratios (R = r_L/r_S) data from Meng et al. (2014). X-large, is = $N_LV_L/(N_LV_L + N_SV_S)$ where N is the number of spheres, V is the volume and the subscripts L and S stand for large and small spheres respectively.

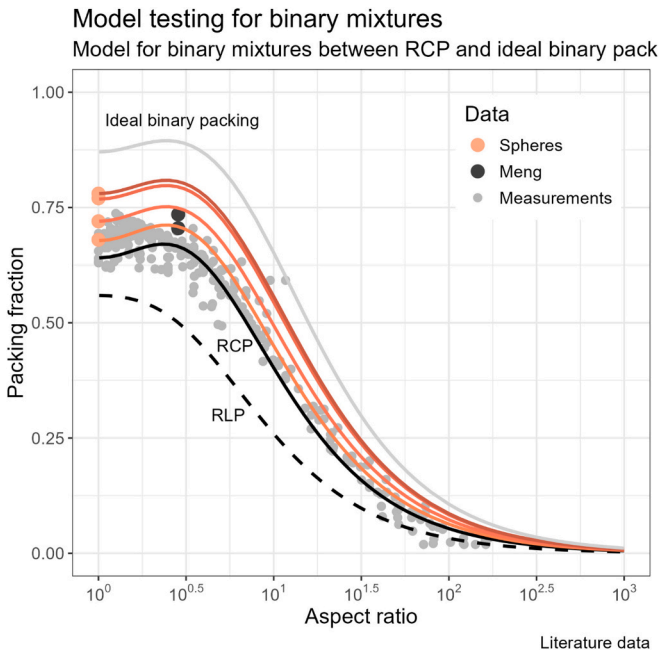

Fig. 14. The alteration of the packing fraction for binary mixtures of particles with different aspect ratios. The black lines represent the dense (RCP) and loose (RLP) packings of monosized prolate particles based on Eq. (13). The grey solid circles are packing data from measurements and simulations found in the literature for monosized particles of different aspect ratio. The salmon-colored solid circles are the packing fractions of binary mixtures of spheres for the size ratios of 2, 3.3, 6.4 and 10.2 in Table 4. The pale grey line is the maximum packing fraction according to the ideal binary packing model. The coral-colored lines represent size ratios of our estimate of the maximum packing response for a size ratio of 2,3,6, and 10, with 2 at the bottom and 10 at the top. The solid black circles represent computer simulations for packings of spherocylinders of aspect ratio 2.85 and size ratio 2 (lower) and 3 (upper) performed by Meng et al. (2012).

⟨C⟩ exhibited an initial decline to approximately 4 within a small size fraction range of 0 to 0.2, followed by a rapid recovery to the original ⟨C⟩ value around a fraction of about 0.3. This phenomenon was similarly noted in modeling efforts by Meng et al. (2014). The extent of the dip in contact numbers is influenced by the size ratio, with a size ratio of approximately 10 resulting in a minimum ⟨C⟩ of about 2.0 before a swift recovery occurs (see Fig. 13). Such low contact number values pose a conceptual challenge, particularly when considering the data presented in Table 1, which indicates that contact numbers around 2 are associated with extremely low packing fractions and the formation of filaments, rather than with dense packing configurations. Furthermore, the steric factor remains to be determined, necessitating further investigation.

It is valuable to assess the potential impact of particle size on Eq.

Table 4
Packing metrics for binary mixtures of spheres based on the data (Table 2) of Kwan et al. (2013). f is the multiplier to obtain an estimate of the maximum packing fraction for a binary mixture with the same aspect ratio but different size ratios given in the first column. The first row represents RCP and the final row is for ideal binary packing with an infinitely large difference in size ratio.

Size ratio	Fraction increase in packing density (PD)	Maximum Packing fraction η_{max}	f
1 RCP	1.00	0.64	0.000
2	1.06	0.68	0.165
3.3	1.13	0.72	0.347
6.4	1.20	0.77	0.556
10.2	1.22	0.78	0.608
∞ Ideal	1.36	0.87	1.000

(13), particularly in the context of densely packed arrangements of both spherical and non-spherical particles. An empirical methodology is suggested to establish potential limits on the anticipated effects. The lower limit is defined by the random close packing (RCP) of monosized particles, illustrated by the solid black line in Fig. 14. To determine an upper limit, we revert to the ideal binary packing model, where the maximum packing fraction is given by $\eta_{max} = (\eta_{small} + \eta_{large})\text{-}(\eta_{small} \times \eta_{large})$. As noted by (Kyrylyuk and Philipse, 2011), in scenarios involving infinite or significantly large size ratios, the packing of various sizes operates independently, without geometrical interference affecting the packing of other size fractions. In this arrangement, larger particles become jammed while smaller particles occupy the spaces between them, effectively filling the voids. Consequently, for a specified relative volume fraction of larger particles, the packing fraction of these larger particles remains unchanged with the introduction of smaller particles, due to the decoupling of length scales. Thus, the packing fraction of the large and small particles is determined from $\eta_{max} = (\eta_{small} + \eta_{large})\text{-}(\eta_{small} \times \eta_{large})$ and independent of the shape of the smaller particles. Therefore, the maximum packing fraction derived from the ideal binary packing model serves as a reasonable theoretical upper limit for binary mixtures of any geometric configuration. Hence, knowing the packing fraction for the different respective geometries based on Eq. (13) an upper bound, termed the 'ideal binary packing' can be calculated (grey solid line in Fig. 14.); with the coefficients required for the monosized RCP model given in Table 3 (RCP-fitted, C1 = 13.3 and C2 = 65.4).

Estimates of what happens in between these bounds, RCP (lower) and Ideal (upper), can be obtained by assuming a simple calculation, where $\eta_{RCP}+((\eta_{Ideal}\text{-}\eta_{RCP})\times\text{fraction } (f))$. Where the fraction ($f$) lies between 0 and 1and is calculated for any size ratio based on the measured packing fraction for binary spheres. $\eta_{RCP}+((\eta_{Ideal}\text{-}\eta_{RCP})\times f)$ = binary mixture packing fraction, and a solver can be used to determine the respective values for different size ratios (Table 4). The size ratio's in Table 4 are plotted in Fig. 14 by lines that are an increasingly deeper shade of coral as the size ratio increases towards that of the ideal binary packing upper bound.

To the best of our knowledge, there is currently no experimental data available to evaluate which curves more accurately represent the correct behavior for non-spheres. Nevertheless, Meng et al. (2012) have recently conducted computer simulations of binary packings composed of spherocylinders. In their study, they highlight that binary packings can include shapes that share the same volume, aspect ratio, or diameter. The focus of their research is on packings with identical aspect ratios, for which they reported a packing fraction of $\eta \approx 0.74$, utilizing an aspect ratio of 2.85 and a size ratio of 2 and 3 (represented by solid black circles). The simulation results align with the coral-colored lines estimated for size ratios of 2 and 3. Consequently, it seems feasible to apply these curves to binary mixtures of non-spherical particles with different aspect ratios, allowing for an estimation of the potential influence of particle size alongside shape considerations.

8. Modeling the bulk density of soils

The bulk density of soils can be modeled using a 2-component mixing approach (Adams, 1973; Robinson et al., 2022; Ruehlmann and Körschens, 2009):

$$\frac{1}{\rho_b} = \frac{SOM}{\rho_{bOM}} + \frac{1 - SOM}{\rho_{bM}} \tag{16}$$

Soil organic matter (SOM) represents the mass fraction of organic material within the soil, while 1-SOM denotes the fraction consisting of mineral matter. The bulk density of pure organic matter is denoted as ρ_{bOM} whereas ρ_{bM} refers to the bulk density of mineral matter. Furthermore, Robinson et al. (2022) modified Eq. (16) to include a grain-scale representation of the bulk density of these components by integrating Song's equation of state (Song et al., 2008). By utilizing Eq. (1), the bulk density can be expressed as the product of the packing fraction and the corresponding particle density, represented as $\rho_b = \eta\rho_s$. Substituting Eq. (12) into this expression yields a revised version of Eq. (16), which establishes a relationship between macroscopic bulk density and the microscopic properties of the particle arrangement.

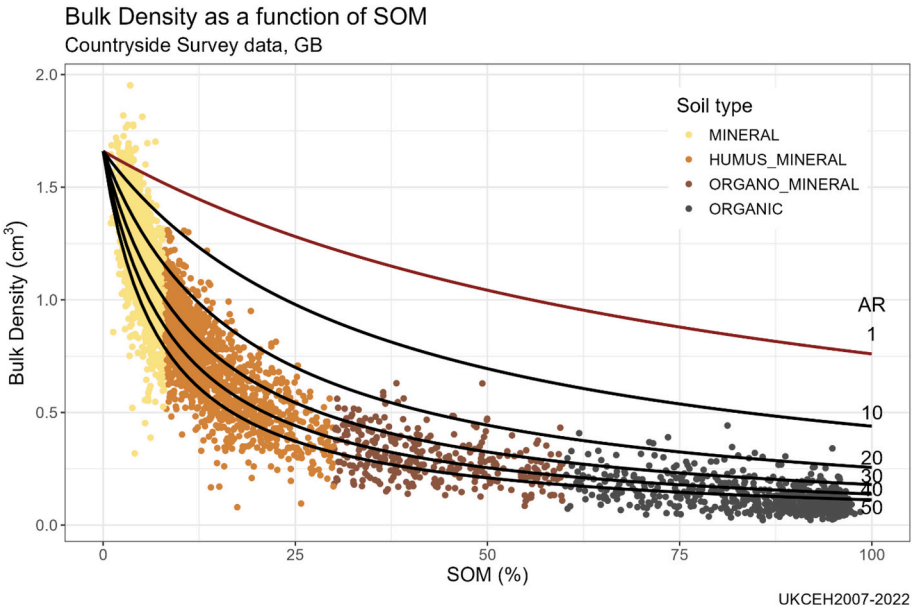

Fig. 15. The bulk density of soils from stratified random monitoring across GB (n = 4202) colored by their organic matter group. The red line represents the bulk density predicted based on the packing of monosized spheres (Eq. (17)) (aspect ratio 1) for the particle density of mineral (2.7 g cm^{-3}) and organic components (1.4 g cm^{-3}) (Ruehlmann, 2020; Ruehlmann and Körschens, 2020). The aspect ratio of the organic part is increased from 10 to 50 (C_1 = 10, C_2 = 45.4, in Eq. (12), between dense and loose for all lines), and v/V_{ex} calculated for prolate particles (Table 2). A value of ~40 has been observed in fibrous peat (Kettridge and Binley, 2011). Bulk density of the mineral fraction 1.66 g cm^{-3}. (For interpretation of the references to colour in this figure legend, the reader is referred to the web version of this article.)

Table 5
Calculations to determine the packing fraction, porosity and bulk density of particles with different aspect ratios (the first line for a sphere, the next 5 lines for prolate particles and the final one for oblate particles). The exclusion fraction is calculated from the prolate equation in Table 2. When the axes a and c are kept constant and only b changes the volume of the prolates increases, but the volume of the oblates decreases, as the AR increases.

Aspect ratio	Prolate spheroid Semiaxis a	Prolate spheroid Semiaxis b	b/a	$e^2 = 1-(a/b)^2$ a = c, b ≥ a	Exclusion fraction V_{ex}/v	Volume	Packing fraction	Porosity	Bulk density
AR = 1.0	1	1.0	1.0	0.0	8.00	4.18	0.54	0.46	0.76
AR = 10	1	10	10	0.9900	26.38	9.06	0.31	0.69	0.44
AR = 20	1	20	20	0.9975	49.61	10.88	0.18	0.82	0.26
AR = 30	1	30	30	0.9988	73.04	12.94	0.13	0.87	0.18
AR = 40	1	40	40	0.9993	96.53	17.31	0.10	0.90	0.14
AR = 50	1	50	50	0.9996	120.05	21.79	0.08	0.92	0.11
AR = 0.055	1	0.055	0.055	0.9969	45.36	0.2303	0.20	0.80	0.54

$$\rho_b = \frac{1}{\frac{SOM}{\rho_{sOM}\left(C_1\left(\frac{v}{V_{ex}}\right) - C_2\left(\frac{v}{V_{ex}}\right)^2_{OM}\right)} + \frac{1-SOM}{\rho_{sM}\left(C_1\left(\frac{v}{V_{ex}}\right) - C_2\left(\frac{v}{V_{ex}}\right)^2_{M}\right)}} \quad (17)$$

Eq. (17) represents a macroscopic arrangement of a phase-separated particle system (Opdam et al., 2022). For instance, this can be illustrated by a layer composed of mineral particles juxtaposed with a layer of soil organic matter (SOM) particles, each serving as a pure end member. The model's predictions are evaluated against the national monitoring data from the UK's Countryside Survey (Reynolds et al., 2013) as depicted in Fig. 15. The particle density values utilized are sourced from Robinson et al. (2022) and informed by the research of Ruehlmann and Körschens (2009), with $\rho_{sOM} = 1.4$ g cm^{-3}, and $\rho_{sM} = 2.7$ g cm^{-3}. The bulk density of mineral particles is calculated as $\rho_{bM} = \rho_{sM} \times \eta_M = 2.7$ (g cm^{-3}) × 0.61 (cm^3 cm^{-3}) = 1.66 g cm^{-3}, as shown in Fig. 15; where 0.61 (cm^3 cm^{-3}) is typical of sand, packing slightly less densely than spheres (0.64). The value for bulk density of the organic matter was predicted using the (V_{ex}/v) for the prolate aspect ratios (10,20,30,40 & 50) (Table 5), where, $\rho_{bOM} = [(10/(V_{ex}/v)) - (45.4/(V_{ex}/v)^2)] \times 1.4$, (OM PD 1.4 g cm^{-3}). Fig. 15 underscores the significance of incorporating the geometrical properties of the particles, where the constants don't change, and the excluded volume is the only thing changing with shape. The red line in Fig. 15 illustrates the predicted bulk density response (Eq. (17)) as organic matter increases, assuming an aspect ratio of 1. This scenario pertains to a mixture of spheres with defined mineral and organic particle densities. The model (Eq. (17)) begins to align with the data only when the aspect ratio is increased. There is limited information regarding the aspect ratio of fibers in peat; however, Kettridge and Binley (2011) investigated the fiber characteristics of peat from Northern England and reported aspect ratios of approximately 40. Modifying the aspect ratio of the organic component in the model to values of 40 and 50 yields highly plausible response curves.

The identical model (Eq. (17)) can be utilized to derive alternative predictions (Fig. 16). Oblate particles, representing clay minerals (aspect ratio = 0.055), are combined with prolate particles, which correspond to organic matter (aspect ratio = 40). The aspect ratio for clay minerals aligns with typical values observed in the literature for low aspect ratio minerals such a mica or kaolinite of 0.033–0.1 (Pabst et al., 2000). This results in a reduction of the mineral component of the response curve, indicating that the oblate particles are positioned in the lower left quadrant of the graph.

Ruehlmann (2020) demonstrated that the model presented in Eq. (16) can be readily adapted to incorporate various components (mineral and organic) for particle density, which holds for bulk density also. Such components may possess distinct geometrical configurations either through shape or size distribution. An estimation of the impact of particle size distribution can be made using the same approach as in Fig. 14 for the ideal binary packing fraction. In the case of monosized spheres RCP is about 0.64 and a binary mixture of spheres with a size ratio of 10

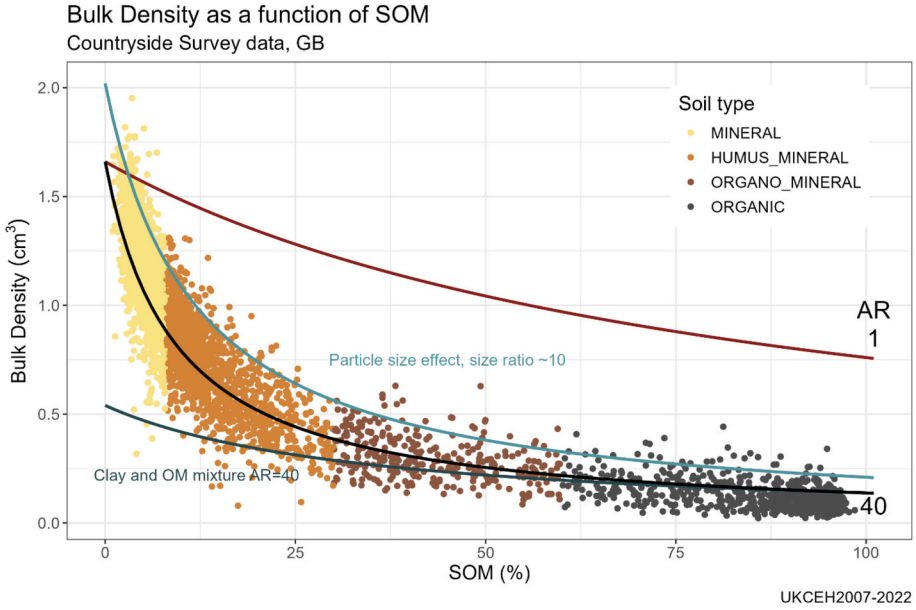

Fig. 16. Countryside survey data with empirical model predictions for mineral and organic mixtures of spheres (AR = 1, dark red line); mineral spheres and prolates (AR = 40, black line); clay (AR = 0.055) mixed with organic matter (AR = 40) dark grey line and particle size distribution effect estimated as a potential limit for end members with binary packing for mineral spheres and organic prolates (AR = 40, pale blue line) assuming a binary particle size ratio of about 10. (For interpretation of the references to colour in this figure legend, the reader is referred to the web version of this article.)

have a maximum packing density of about 0.78 (Fig. 14), i.e. a 22 % higher packing fraction (Fig. 16). In the case of monosized prolate particles with an aspect ratio of 40 the packing fraction is 0.1 and the porosity 0.9, so that with a particle density of 1.4 g cm^{-3} the bulk density is about 0.14 g cm^{-3} (Table 5). Knowing these values and the fractional increase for a binary mixture of spheres or prolates with a size ratio of about 10 the respective maximum packing fractions can be calculated. For a binary mixture of prolate particles with AR = 40 the ideal packing fraction is $\eta_{max} = (\eta_{small} + \eta_{large})-(\eta_{small} \times \eta_{large}) = (0.1 + 0.1)-(0.1 \times 0.1) = 0.19$ for an infinite size ratio difference. For a size ratio of 10 the maximum packing fraction is $= \eta_{RCP}+((\eta_{Ideal}-\eta_{RCP})$ *fraction) $= 0.1 + (0.19–0.1) \times 0.608 = 0.155$, where the fraction is from column 4 in Table 4. Hence, the ratio 0.155/0.1 = 1.55, so about 55 % higher for the binary mixture of prolates. So that the bulk density of the end members increases from 1.66 for mineral particles to $1.66 \times 1.22 = 2.03$ g cm^{-3} and the bulk density of the prolate end member increases from $0.138 \times 1.55 = 0.21$ g cm^{-3}; this is shown as the pale blue line in Fig. 16. What the line indicates is that compared to shape effects, particle size effects are relatively small. The above evaluation is an upper bound to the effect of (a large) 10:1 size ratio mixture, since it is for the maximum increase obtained in a particular volumetric fractional composition of approximately 1/3 small and 2/3 large particles. The point being that simply increasing the size distribution has a limited effect on densification and is not the only factor that might result in denser materials. Factors such as preferential grain orientation in the case of organic materials and compaction may become much more significant. Factors such as particle orientation, tendency towards an aligned nematic phase, or compaction should be considered for data falling above this line in addition to shape effects. In addition, characteristics such as aggregation which is clearly related to total porosity in minerals soils (Thomas et al., 2024) and the fact that organic matter is not rigid and can absorb water are also not considered. Also (smectite) clay tactoids can swell and reduce the bulk density, as well as interfacial forces. In contrast capillary forces may increase the bulk density. Furthermore, Fig. 16 illustrates the model representation of a mixture of clay and organic matter (depicted by the slate grey line) alongside data from GB (n = 4202). The models presented in this work indicate that the emergent bulk density is a combination of grain scale characteristics.

9. General discussion

The mixing model approach for soils discussed in this study appears to have been initially introduced by (Adams, 1973) and has since been adapted in various forms by numerous researchers, including (Hallett et al., 1998; Robinson et al., 2022; Ruehlmann, 2020; Ruehlmann and Körschens, 2009; Ruehlmann and Körschens, 2020; Tranter et al., 2007). This research aims to enhance both the conceptual and physical comprehension of how macroscale responses are linked to microscale characteristics. The methodologies outlined primarily concentrate on the influence of the solid phase components of soil—specifically their size, shape, and particle density—on the porosity and bulk density of natural soils. However, this work does not address additional factors that may influence soil bulk density, such as seasonal cycles of soil shrinkage and swelling, nor does it consider the processes of compaction and loosening, whether anthropogenic or natural. Historically, much of the environmental soil literature has concentrated on developing models for bulk density and porosity through the application of statistical functions to various data sets (Botula et al., 2015; Heuscher et al., 2005; Hollis et al., 2012; Kaur et al., 2002; Manrique and Jones, 1991; Martín et al., 2017; Nemes et al., 2010; Panagos et al., 2024; Ramcharan et al., 2017; Rodríguez-Lado et al., 2015; Thomas et al., 2024; Tranter et al., 2007). A significant challenge associated with fitting statistical functions is that the results are contingent upon the data utilized. Many extensive data sets are incomplete regarding the full environmental range of soil bulk density. The UKCEH Countryside Survey data (Reynolds et al., 2013), employed in this study, serves as a valuable resource for testing due to its stratified random design, which provides comprehensive coverage of changes in soil organic matter (SOM) across a latitudinal gradient where SOM ranges from approximately 0 % to 100 %. Additionally, the new LUCAS data set (Panagos et al., 2024) for Europe is beneficial, although it is limited in its representation of highly organic-rich soils.

Bulk density, often regarded as a static parameter, has been shown to exhibit variability on anthropogenic time scales throughout the United States (Hirmas et al., 2018). Additionally, research indicates that this property is subject to seasonal fluctuations (Hu et al., 2012; Wuest, 2015). The findings of Hirmas et al. (2018) highlighted several critical issues, particularly concerning the influence of continental-scale changes, driven by unidentified mechanisms, on the hydrological cycle. Recent investigations have sought to elucidate the mechanisms governing bulk density and porosity, with land cover and complexed clay identified as significant factors at national and broader scales (Koop et al., 2023; Panagos et al., 2024; Thomas et al., 2024). Both studies underscore the pivotal role of organic matter, as indicated by land cover variations. Furthermore, Thomas et al. (2024) explored whether integrating soil organic matter (SOM) with habitat data enhanced predictive accuracy. While habitat contributed minimally but significantly to the predictions, the majority of the predictive strength was attributed to SOM. This suggests that SOM likely reflects the impacts of geometric changes induced by plant roots, litter, and fungi, among other factors.

The significant correlation between bulk density and soil organic matter (SOM) indicates that land management practices influencing SOM will also affect bulk density. This relationship is particularly pronounced in temperate and northern latitude soils, where SOM plays a crucial role in determining bulk density. Research has demonstrated that SOM levels fluctuate in response to changes in land use (Guo and Gifford, 2002) suggesting that bulk density is likely to exhibit similar variations. Over the past four decades, numerous national surveys have documented a decrease in SOM within cropland soils (Bellamy et al., 2005). Based on the findings presented in this study, any decline in organic matter is anticipated to result in increased soil bulk density. The reduction of SOM will have repercussions on both the structural integrity of soil aggregates (Sullivan et al., 2022) and the overall geometry of soil particles, as soils tend to transition towards materials characterized by a lower aspect ratio.

Restoring soil structure poses a significant practical challenge. This synthesis provides valuable insights into this issue. The incorporation of mineral and soil organic matter (SOM) components alters the evaluation of bulk density due to the inherent differences in particle densities. However, achieving further improvements necessitates that these components possess distinct geometrical characteristics. Elements such as roots, fungal hyphae, and organic litter can modify the geometry of the soil mixture. Their presence can further reduce bulk density, attributable to their greater aspect ratios compared to granular mineral materials alone. In contrast, root exudates may not influence soil geometry directly but can exert a dual opposing effect. They may facilitate dispersion, leading to reduced aggregation, or enhance the ‘stickiness’ that promotes aggregate formation (Sullivan et al., 2022). Therefore, strategies that involve the addition of SOM, the incorporation of roots, or the use of cover crops, along with mixing facilitated by organisms such as earthworms, can significantly contribute to soil restoration, provided the soil is not excessively compacted. The sequence of restoration activities is also crucial. Initially, some form of mechanical intervention may be necessary to loosen the soil, followed by the incorporation of organic matter and planting to ensure that roots support the developing structure. The role of soil biota, particularly earthworms, should not be overlooked, as they are essential for both mixing and maintaining soil structure (Blanchart et al., 1999; Hallam et al., 2021; Shipitalo and Le Bayon, 2004; Yvan et al., 2012). Implementing cover cropping will help maintain root systems and prevent the soil from reverting to a more compacted condition.

Numerous studies have examined the influence of bulk density on

root development. However, literature specifically addressing the reciprocal effects of roots on bulk density is relatively scarce; most research tends to concentrate on broader aspects of soil structure (Angers and Caron, 1998) or hydraulic properties (Lu et al., 2020). Recent investigations have sought to integrate biological influences on soil structure into innovative dynamic water retention models (Meurer et al., 2020). The current study contributes a conceptual advancement that complements these initiatives. A notable finding is that fine roots often obstruct pore spaces, utilizing existing voids rather than generating new ones, while larger woody roots are more likely to fracture the soil and foster new structural formations (Lu et al., 2020; Meurer et al., 2020). This indicates that woody species may be more effective in enhancing soil structure compared to herbaceous plants, potentially leading to more enduring alterations in bulk density. Furthermore, the diversity of root systems may also play a role in influencing bulk density. It can be inferred that biodiverse plant communities, characterized by a variety of root shapes and sizes, could reduce bulk density by creating greater disturbances in soil packing. Empirical support for this notion is found in studies of saltmarsh ecosystems, which demonstrate that increased plant diversity, and consequently root diversity, correlates with reduced erosion (Ford et al., 2016). Therefore, while the present work sheds light on the impact of particle morphology on packing, there remains a significant scope for further investigation, particularly concerning the interactions between biological factors and abiotic particles that culminate in soil bulk density as an emergent characteristic.

10. Conclusions

Soil bulk density is influenced by the particle density of soil constituents and their geometric characteristics, including shape and size ratio. The shape of particles, particularly platy clay minerals which can be represented as oblate spheroids, and fibrous organic matter, originally root materials, modeled as prolate particles, plays a significant role in this relationship. An understanding of how macroscopic properties like bulk density and porosity relate to microscale features such as particle shape (aspect ratio), contact number, and the effects of excluded volume—especially as particle aspect ratios deviate from unity—provides critical insights. An empirical model that incorporates contact number, excluded volume, and steric effects effectively captures the packing behavior of various particle types, including platy, granular, and rod-shaped forms. When integrated into a macroscopic mixing model, these factors enhance our comprehension and quantification of soil bulk density. Practically, this indicates that managing soil bulk density involves not only adjusting the proportions of mineral and organic components but also addressing the overall geometry of the soil system. In essence, the shape of solid particles is crucial in the management or restoration of soil bulk density. Soils with particles exhibiting a higher aspect ratio tend to experience less natural densification. Consequently, while the density of added organic matter contributes to a reduction in bulk density, the particle shape of these organic materials is equally important. Furthermore, the depletion of organic matter, particularly in fibrous forms, can result in increased natural densification. It is important to note that no amount of tillage can permanently restore soil structure unless the geometry of the soil is also reinstated. These findings may facilitate the development of innovative techniques for soil structure restoration and provide valuable insights into the interactions between climate, soil carbon, and soil structure on a broader scale.

Author contributions statement

DAR handled the conceptualization and writing – original draft, SF, AT, DH, PO, and AN were responsible for review & editing. AN, DH, PO and DAR handled the funding acquisition.

During the preparation of this work the author(s) used ahrefs sentence rewriting tool in order to improve the consistency of the language across multiple international authors. After using this tool, the authors reviewed and edited the content as needed and take full responsibility for the content of the publication.

Funding

The research was funded by the

- The Research Council of Norway, Climasoil, Project number: 325253.
- This research was supported/partially supported by NERC, through the UKCEH National Capability for UK Challenges Programme NE/Y006208/1.
- This project acknowledges funding from the European Union's Horizon Europe research and innovation program under grant agreement No.-101086179; and funding from the UK Research and Innovation (UKRI) under the UK government's Horizon Europe funding guarantee [grant number 10053484] as part of AI4SoilHealth.

Declaration of competing interest

The authors declare that they have no known competing financial interests or personal relationships that could have appeared to influence the work reported in this paper.

Acknowledgments

General: We thank all the UKCEH Countryside Survey team who collected all the data from England, Wales and Scotland. Disclaimer: Work funded by the European Union. Views and opinions expressed are however those of the author(s) only and do not necessarily reflect those of the European Union or the Research Executive Agency. Neither the European Union nor the granting authority can be held responsible for them.

Data availability

All data is openly available in the literature

References

Adams, W., 1973. The effect of organic matter on the bulk and true densities of some uncultivated podzolic soils. J. Soil Sci. 24 (1), 10–17.
An, X., Yang, R., Zou, R., Yu, A., 2008. Effect of vibration condition and inter-particle frictions on the packing of uniform spheres. Powder Technol. 188 (2), 102–109.
Angers, D.A., Caron, J., 1998. Plant-induced changes in soil structure: processes and feedbacks. Biogeochemistry 42, 55–72.
Anstreicher, K.M., 2004. The thirteen spheres: a new proof. Discrete Comput. Geom. 31, 613–625.
Aste, T., Weaire, D., 2008. The Pursuit of Perfect Packing. CRC Press.
Aste, T., Saadatfar, M., Sakellariou, A., Senden, T.J., 2004. Investigating the geometrical structure of disordered sphere packings. Physica A 339 (1–2), 16–23.
Aste, T., Saadatfar, M., Senden, T., 2005. Geometrical structure of disordered sphere packings. Phys. Rev. E 71 (6), 061302.
Atwood, T.B., Witt, A., Mayorga, J., Hammill, E., Sala, E., 2020. Global patterns in marine sediment carbon stocks. Front. Mar. Sci. 7, 165.
Avnimelech, Y., Ritvo, G., Meijer, L.E., Kochba, M., 2001. Water content, organic carbon and dry bulk density in flooded sediments. Aquac. Eng. 25 (1), 25–33.
Bellamy, P.H., Loveland, P.J., Bradley, R.I., Lark, R.M., Kirk, G.J.D., 2005. Carbon losses from all soils across England and Wales 1978-2003. Nature 437 (7056), 245–248.
Bennett, C.H., 1972. Serially deposited amorphous aggregates of hard spheres. J. Appl. Phys. 43 (6), 2727–2734.
Bernal, J.D., Mason, J., 1960. Packing of spheres: co-ordination of randomly packed spheres. Nature 188 (4754), 910–911.
Bezdek, K., Khan, M.A., 2018. Contact numbers for sphere packings. In: New Trends in Intuitive Geometry, pp. 25–47.
Blake, G.R., Hartge, K., 1986. Bulk Density. Methods of Soil Analysis: Part 1 Physical and Mineralogical Methods, 5, pp. 363–375.
Blanchart, E., Albrecht, A., Alegre, J., Duboisset, A., Gilot, C., Pashanasi, B., Lavelle, P., Brussaard, L., 1999. Effects of earthworms on soil structure and physical properties. In: Earthworm Management in Tropical Agroecosystems, 5, pp. 149–171.

Borrelli, P., Robinson, D.A., Fleischer, L.R., Lugato, E., Ballabio, C., Alewell, C., Meusburger, K., Modugno, S., Schütt, B., Ferro, V., 2017. An assessment of the global impact of 21st century land use change on soil erosion. Nat. Commun. 8 (1), 2013.
Botula, Y.-D., Nemes, A., Van Ranst, E., Mafuka, P., De Pue, J., Cornelis, W.M., 2015. Hierarchical pedotransfer functions to predict bulk density of highly weathered soils in Central Africa. Soil Sci. Soc. Am. J. 79 (2), 476–486.
Brouwers, H., 2013. Random packing fraction of bimodal spheres: An analytical expression. Phys. Rev. E 87 (3), 032202.
Conway, J.H., Sloane, N.J.A., 2013. Sphere Packings, Lattices and Groups, 290. Springer Science & Business Media.
Cumberland, D., Crawford, R.J., 1987. The packing of particles. In: Handbook of Powder Technology, 6. Elsevier, Amsterdam.
de Lange Kristiansen, K., Wouterse, A., Philipse, A., 2005. Simulation of random packing of binary sphere mixtures by mechanical contraction. Physica A 358 (2–4), 249–262.
Delaney, G.W., Di Matteo, T., Aste, T., 2010. Combining tomographic imaging and DEM simulations to investigate the structure of experimental sphere packings. Soft Matter 6 (13), 2992–3006.
Dias, R.P., Teixeira, J.A., Mota, M.G., Yelshin, A.I., 2004. Particulate binary mixtures: dependence of packing porosity on particle size ratio. Ind. Eng. Chem. Res. 43 (24), 7912–7919.
Dippenaar, M.A., 2014. Porosity reviewed: quantitative multi-disciplinary understanding, recent advances and applications in vadose zone hydrology. Geotech. Geol. Eng. 32 (1), 1–19.
Donev, A., 2006. PhD Jammed Packings of Hard Particles. Princeton University.
Donev, A., Cisse, I., Sachs, D., Variano, E.A., Stillinger, F.H., Connelly, R., Torquato, S., Chaikin, P.M., 2004. Improving the density of jammed disordered packings using ellipsoids. Science 303 (5660), 990–993.
Dor, M., Levi-Kalisman, Y., Day-Stirrat, R.J., Mishael, Y., Emmanuel, S., 2020. Assembly of clay mineral platelets, tactoids, and aggregates: effect of mineral structure and solution salinity. J. Colloid Interface Sci. 566, 163–170.
Farr, R.S., Groot, R.D., 2009. Close packing density of polydisperse hard spheres. J. Chem. Phys. 131 (24).
Finney, J., 1970. Random packings and the structure of simple liquids. I. The geometry of random close packing. Proc. Roy. Soc. Lond. A 319 (1539), 479–493.
Flint, L.E., Flint, A.L., 2002. 2.3 Porosity. In: Methods of Soil Analysis: Part 4 Physical Methods, 5, pp. 241–254.
Ford, H., Garbutt, A., Ladd, C., Malarkey, J., Skov, M.W., 2016. Soil stabilization linked to plant diversity and environmental context in coastal wetlands. J. Veg. Sci. 27 (2), 259–268.
Furnas, C., 1931. Grading aggregates-I.-Mathematical relations for beds of broken solids of maximum density. Ind. Eng. Chem. 23 (9), 1052–1058.
Gan, J., Yu, A., 2020. DEM study on the packing density and randomness for packing of ellipsoids. Powder Technol. 361, 424–434.
Gan, J., Yu, A., Zhou, Z., 2016. DEM simulation on the packing of fine ellipsoids. Chem. Eng. Sci. 156, 64–76.
Gardner, M., 1966. "Packing spheres" Martin Gardner's new mathematical diversions from Scientific American. Sci. Am. 82–90.
González García, A., 2015. Random Packings Via Mechanical Contraction (Masters Thesis). Utrecht University.
González-Teruel, J.D., Jones, S.B., Soto-Valles, F., Torres-Sánchez, R., Lebron, I., Friedman, S.P., Robinson, D.A., 2020. Dielectric spectroscopy and application of mixing models describing dielectric dispersion in clay minerals and clayey soils. Sensors 20 (22), 6678.
Grossman, R., Reinsch, T., 2002. 2.1 Bulk density and linear extensibility. In: Methods of Soil Analysis: Part 4 Physical Methods, vol. 5, pp. 201–228.
Guo, L.B., Gifford, R.M., 2002. Soil carbon stocks and land use change: a meta analysis. Glob. Chang. Biol. 8 (4), 345–360.
Hales, T., Adams, M., Bauer, G., Dang, T.D., Harrison, J., Le Truong, H., Kaliszyk, C., Magron, V., McLaughlin, S., Nguyen, T.T., 2017. A Formal Proof of the Kepler Conjecture, Forum of Mathematics, Pi. Cambridge University Press.
Hallam, J., Holden, J., Robinson, D.A., Hodson, M.E., 2021. Effects of winter wheat and endogeic earthworms on soil physical and hydraulic properties. Geoderma 400, 115126.
Hallett, S., Hollis, J., Keay, C., 1998. Derivation and Evaluation of a Set of Pedogenically-Based Empirical Algorithms for Predicting Bulk Density in British Soils.
Heuscher, S.A., Brandt, C.C., Jardine, P.M., 2005. Using soil physical and chemical properties to estimate bulk density. Soil Sci. Soc. Am. J. 69 (1), 51–56.
Hirmas, D.R., Giménez, D., Nemes, A., Kerry, R., Brunsell, N.A., Wilson, C.J., 2018. Climate-induced changes in continental-scale soil macroporosity may intensify water cycle. Nature 561 (7721), 100.
Hollis, J., Hannam, J., Bellamy, P., 2012. Empirically-derived pedotransfer functions for predicting bulk density in European soils. Eur. J. Soil Sci. 63 (1), 96–109.
Hopkins, A.B., Jiao, Y., Stillinger, F.H., Torquato, S., 2011. Phase diagram and structural diversity of the densest binary sphere packings. Phys. Rev. Lett. 107 (12), 125501.
Hopkins, A.B., Stillinger, F.H., Torquato, S., 2012. Densest binary sphere packings. Phys. Rev. E 85 (2), 021130.
Hossain, M., Chen, W., Zhang, Y., 2015. Bulk density of mineral and organic soils in the Canada's arctic and sub-arctic. Inform. Process. Agric. 2 (3–4), 183–190.
Hu, W., Shao, M., Si, B., 2012. Seasonal changes in surface bulk density and saturated hydraulic conductivity of natural landscapes. Eur. J. Soil Sci. 63 (6), 820–830.
Isola, R., 2008. Packing of Granular Materials. University of Nottingham Nottingham, England.
Jacquelin, J., 2024. How to combine properties of different functions into a new function? URL (version: 2018-10-24). https://stats.stackexchange.com/q/373387.
Jia, M., Xu, W., Zhu, Z., 2019. Numerical study on the excluded volumes of realistic 3D non-convex particles. Powder Technol. 349, 52–58.
Kaur, R., Kumar, S., Gurung, H., 2002. A pedo-transfer function (PTF) for estimating soil bulk density from basic soil data and its comparison with existing PTFs. Soil Res. 40 (5), 847–858.
Keller, T., Håkansson, I., 2010. Estimation of reference bulk density from soil particle size distribution and soil organic matter content. Geoderma 154 (3–4), 398–406.
Kepler, J., 1966. Strena Seu de Niue Sexangula. Gottfried Tampach.
Kettridge, N., Binley, A., 2011. Characterization of peat structure using X-ray computed tomography and its control on the ebullition of biogenic gas bubbles. J. Geophys. Res. Biogeosci. 116 (G1).
Kojima, Y., Heitman, J.L., Sakai, M., Kato, C., Horton, R., 2018. Bulk density effects on soil hydrologic and thermal characteristics: a numerical investigation. Hydrol. Process. 32 (14), 2203–2216.
Koltermann, C.E., Gorelick, S.M., 1995. Fractional packing model for hydraulic conductivity derived from sediment mixtures. Water Resour. Res. 31 (12), 3283–3297.
Koop, A.N., Hirmas, D.R., Billings, S.A., Li, L., Cueva, A., Zhang, X., Wen, H., Nemes, A., Souza, L.F., Ajami, H., 2023. Is macroporosity controlled by complexed clay and soil organic carbon? Geoderma 437, 116565.
Kravchenko, A., Guber, A., Razavi, B., Koestel, J., Quigley, M., Robertson, G., Kuzyakov, Y., 2019. Microbial spatial footprint as a driver of soil carbon stabilization. Nat. Commun. 10 (1), 3121.
Kwan, A.K.H., Chan, K.W., Wong, V., 2013. A 3-parameter particle packing model incorporating the wedging effect. Powder Technol. 237, 172–179.
Kyrylyuk, A.V., Philipse, A.P., 2011. Effect of particle shape on the random packing density of amorphous solids. Phys. Status Solidi A 208 (10), 2299–2302.
Lee, J., Hopmans, J.W., Rolston, D.E., Baer, S.G., Six, J., 2009. Determining soil carbon stock changes: simple bulk density corrections fail. Agric. Ecosyst. Environ. 134 (3–4), 251–256.
Lemaitre, J., Troadec, J., Bideau, D., Gervois, A., Bougault, E., 1988. The formation factor of the pore space of binary mixtures of spheres. J. Phys. D. Appl. Phys. 21 (11), 1589.
Li, H., 2005. Impact of Cohesion Forces on Particle Mixing and Segregation. University of Pittsburgh.
Liu, L., Zhang, Z., Yu, A., 1999. Dynamic simulation of the centripetal packing of mono-sized spheres. Physica A 268 (3–4), 433–453.
Lu, J., Zhang, Q., Werner, A.D., Li, Y., Jiang, S., Tan, Z., 2020. Root-induced changes of soil hydraulic properties – a review. J. Hydrol. 589, 125203.
Manegold, E., von Engelhardt, W., 1933. Über Kapillar-Systeme, XII (2). Die Berechnung des Stoffgehaltes homogener Gerüststrukturen: Erster Teil. Kugel-Ebenen und Kugel-Schichten als Bauelemente homogener Kugel-Gitter. Kolloid-Zeitschrift 62 (3), 285–294.
Manrique, L., Jones, C., 1991. Bulk density of soils in relation to soil physical and chemical properties. Soil Sci. Soc. Am. J. 55 (2), 476–481.
Mansfield, M.L., Rakesh, L., Tomalia, D.A., 1996. The random parking of spheres on spheres. J. Chem. Phys. 105 (8), 3245–3249.
Martín, M.Á., Reyes, M., Taguas, F.J., 2017. Estimating soil bulk density with information metrics of soil texture. Geoderma 287, 66–70.
Mason, G., 1968. Radial distribution functions from small packings of spheres. Nature 217 (5130), 733–735.
Matheson, A., 1974. Computation of a random packing of hard spheres. J. Phys. C Solid State Phys. 7 (15), 2569.
Melnyk, R., Trokhymchuk, A., Baumketner, A., 2022. Excluded volume of the system of hard-core spheres revisited: New insights from computer simulations. J. Mol. Liq. 368, 120672.
Meng, L., Lu, P., Li, S., Zhao, J., Li, T., 2012. Shape and size effects on the packing density of binary spherocylinders. Powder Technol. 228, 284–294.
Meng, L., Lu, P., Li, S., 2014. Packing properties of binary mixtures in disordered sphere systems. Particuology 16, 155–166.
Meurer, K., Barron, J., Chenu, C., Coucheney, E., Fielding, M., Hallett, P., Herrmann, A. M., Keller, T., Koestel, J., Larsbo, M., 2020. A framework for modelling soil structure dynamics induced by biological activity. Glob. Chang. Biol. 26 (10), 5382–5403.
Migal, L., Bondarev, V., Chekanov, N., Bondareva, T., 2020. Simulation of the coordination number of random sphere packing. J. Phys. Conf. Ser. 012097. IOP Publishing.
Mota, M., Teixeira, J., Bowen, W.R., Yelshin, A., 2001. Binary Spherical Particle Mixed Beds: Porosity and Permeability Relationship Measurement.
Nemes, A., Quebedeaux, B., Timlin, D., 2010. Ensemble approach to provide uncertainty estimates of soil bulk density. Soil Sci. Soc. Am. J. 74 (6), 1938–1945.
Neudecker, M., Ulrich, S., Herminghaus, S., Schröter, M., 2013. Jammed frictional tetrahedra are hyperstatic. Phys. Rev. Lett. 111 (2), 028001.
Nimmo, J.R., 2004. Porosity and pore size distribution. Encyclop. Soils Environ. 3 (1), 295–303.
Onsager, L., 1949. The effects of shape on the interaction of colloidal particles. Ann. N. Y. Acad. Sci. 51 (4), 627–659.
Opdam, J., Gandhi, P., Kuhnhold, A., Schilling, T., Tuinier, R., 2022. Excluded volume interactions and phase stability in mixtures of hard spheres and hard rods. Phys. Chem. Chem. Phys. 24 (19), 11820–11827.
Pabst, W., Gregorova, E., 2007. Characterization of particles and particle systems. ICT Prague 122, 122.
Pabst, W., Kuneš, K., Havrda, J., Gregorová, E., 2000. A note on particle size analyses of kaolins and clays. J. Eur. Ceram. Soc. 20 (9), 1429–1437.
Panagos, P., De Rosa, D., Liakos, L., Labouyrie, M., Borrelli, P., Ballabio, C., 2024. Soil bulk density assessment in Europe. Agric. Ecosyst. Environ. 364, 108907.
Percus, J.K., Yevick, G.J., 1958. Analysis of classical statistical mechanics by means of collective coordinates. Phys. Rev. 110 (1), 1.

Philipse, A.P., 1996. The random contact equation and its implications for (colloidal) rods in packings, suspensions, and anisotropic powders. Langmuir 12 (5), 1127–1133.
Pinson, D., Zou, R., Yu, A., Zulli, P., McCarthy, M., 1998. Coordination number of binary mixtures of spheres. J. Phys. D. Appl. Phys. 31 (4), 457.
Planck, M., 1908. Über die kanonische Zustandsgleichung einatomiger Gase. Sitzungsber. Preussische Akad. Wissensch. Berlin 633–647.
Ramcharan, A., Hengl, T., Beaudette, D., Wills, S., 2017. A soil bulk density pedotransfer function based on machine learning: a case study with the NCSS soil characterization database. Soil Sci. Soc. Am. J. 81 (6), 1279–1287.
Reiss, H., Frisch, H., Lebowitz, J., 1959. Statistical mechanics of rigid spheres. J. Chem. Phys. 31 (2), 369–380.
Reynolds, B., Chamberlain, P., Poskitt, J., Woods, C., Scott, W., Rowe, E., Robinson, D., Frogbrook, Z., Keith, A., Henrys, P., 2013. Countryside Survey: National "Soil Change" 1978–2007 for Topsoils in Great Britain—acidity, carbon, and total nitrogen status. Vadose Zone J. 12 (2), 1–15.
Robinson, D.A., Friedman, S.P., 2001. Effect of particle size distribution on the effective dielectric permittivity of saturated granular media. Water Resour. Res. 37 (1), 33–40.
Robinson, D., Thomas, A., Reinsch, S., Lebron, I., Feeney, C., Maskell, L., Wood, C., Seaton, F., Emmett, B., Cosby, B., 2022. Analytical modelling of soil porosity and bulk density across the soil organic matter and land-use continuum. Sci. Rep. 12 (1), 1–13.
Rodríguez-Lado, L., Rial, M., Taboada, T., Cortizas, A.M., 2015. A pedotransfer function to map soil bulk density from limited data. Procedia Environ. Sci. 27, 45–48.
Rotenberg, B., Patel, A.J., Chandler, D., 2011. Molecular explanation for why talc surfaces can be both hydrophilic and hydrophobic. J. Am. Chem. Soc. 133 (50), 20521–20527.
Ruehlmann, J., 2020. Soil particle density as affected by soil texture and soil organic matter: 1. Partitioning of SOM in conceptional fractions and derivation of a variable SOC to SOM conversion factor. Geoderma 375, 114542.
Ruehlmann, J., Körschens, M., 2009. Calculating the effect of soil organic matter concentration on soil bulk density. Soil Sci. Soc. Am. J. 73 (3), 876–885.
Ruehlmann, J., Körschens, M., 2020. Soil particle density as affected by soil texture and soil organic matter: 2. Predicting the effect of the mineral composition of particle-size fractions. Geoderma 375, 114543.
Rusanov, A.I., 2003a. Equation of state theory based on excluded volume. J. Chem. Phys. 118 (22), 10157–10163.
Rusanov, A.I., 2003b. Generalized equation of state and exclusion factor for multicomponent systems. J. Chem. Phys. 119 (19), 10268–10273.
Rusanov, A.I., 2004. Theory of excluded volume equation of state: higher approximations and new generation of equations of state for entire density range. J. Chem. Phys. 121 (4), 1873–1877.
Rusanov, A.I., 2010. Excluded volume: a historical enigma of the van der Waals equation of state. J. Chem. Eng. Data 55 (10), 4176–4182.
Scarlett, B., Van Der Kraan, M., Janssen, R., 1998. Porosity: a parameter with no direction. Philos. Trans. R. Soc. London, Ser. A 356 (1747), 2623–2648.
Scott, G.D., 1962. Radial distribution of the random close packing of equal spheres. Nature 194 (4832), 956–957.
Senetakis, K., Coop, M.R., Todisco, M.C., 2013. The inter-particle coefficient of friction at the contacts of Leighton Buzzard sand quartz minerals. Soils Found. 53 (5), 746–755.
Sherwood, J., 1997. Packing of spheroids in three-dimensional space by random sequential addition. J. Phys. A Math. Gen. 30 (24), L839.
Shipitalo, M.J., Le Bayon, R.-C., 2004. Quantifying the effects of earthworms on soil aggregation and porosity. In: Earthworm Ecology. CRC Press, pp. 183–200.
Sibellas, A., Drummond, J., Martinez, D., Phillion, A., 2024. Connectivity in binary mixtures of spherical particles. Tomogr. Mater. Struct. 100026.
Silbert, L.E., 2010. Jamming of frictional spheres and random loose packing. Soft Matter 6 (13), 2918–2924.
Silbert, L.E., Ertaş, D., Grest, G.S., Halsey, T.C., Levine, D., 2002. Geometry of frictionless and frictional sphere packings. Phys. Rev. E 65 (3), 031304.
Sohn, H.Y., Moreland, C., 1968. The effect of particle size distribution on packing density. Can. J. Chem. Eng. 46 (3), 162–167.
Song, C., Wang, P., Makse, H.A., 2008. A phase diagram for jammed matter. Nature 453 (7195), 629–632.
Sullivan, P.L., Billings, S.A., Hirmas, D., Li, L., Zhang, X., Ziegler, S., Murenbeeld, K., Ajami, H., Guthrie, A., Singha, K., Gimmenez, D., Duro, A., Moreno, V., Flores, A., Cueva, A., Koop, A.N., Aronson, E., Barnard, H., S, B., R, K., H, W., 2022. Embracing the dynamic nature of soil structure: a paradigm illuminating the role of life in critical zones of the Anthropocene. Earth Sci. Rev. 225, 103873.
Thomas, A., Seaton, F., Dhiedt, E., Cosby, B., Feeney, C., Lebron, I., Maskell, L., Wood, C., Reinsch, S., Emmett, B., 2024. Topsoil porosity prediction across habitats at large scales using environmental variables. Sci. Total Environ. 922, 171158.
To, L.T., Stachurski, Z.H., 2004. Random close packing of spheres in a round cell. J. Non-Cryst. Solids 333 (2), 161–171.
Torquato, S., 2012. Effect of dimensionality on the continuum percolation of overlapping hyperspheres and hypercubes. J. Chem. Phys. 136 (5).
Torquato, S., 2013. Random Heterogeneous Materials: Microstructure and Macroscopic Properties, 16. Springer Science & Business Media.
Torquato, S., Jiao, Y., 2013. Effect of dimensionality on the percolation thresholds of various d-dimensional lattices. Phys. Rev. E 87 (3), 032149.
Torquato, S., Jiao, Y., 2022. Exclusion volumes of convex bodies in high space dimensions: applications to virial coefficients and continuum percolation. J. Stat. Mech. 2022 (9), 093404.
Torquato, S., Stillinger, F.H., 2010. Jammed hard-particle packings: from Kepler to Bernal and beyond. Rev. Mod. Phys. 82 (3), 2633.
Torquato, S., Truskett, T.M., Debenedetti, P.G., 2000. Is random close packing of spheres well defined? Phys. Rev. Lett. 84 (10), 2064.
Tranter, G., Minasny, B., McBratney, A., Murphy, B., McKenzie, N., Grundy, M., Brough, D., 2007. Building and testing conceptual and empirical models for predicting soil bulk density. Soil Use Manag. 23 (4), 437–443.
Van der Waals, J.D., 1873. Over de Continuiteit van den Gas-en Vloeistoftoestand, 1. Sijthoff.
Visscher, W.M., Bolsterli, M., 1972. Random packing of equal and unequal spheres in two and three dimensions. Nature 239 (5374), 504–507.
Wang, J., Lei, M., Yang, H., Xu, K., Xu, S., Zhao, P., Song, Y., 2021. Effects of coefficient of friction and coefficient of restitution on static packing characteristics of polydisperse spherical pebble bed. Particuology 57, 1–9.
Weitz, D.A., 2004. Packing in the spheres. Science 303 (5660), 968–969.
Widom, B., 1966. Random sequential addition of hard spheres to a volume. J. Chem. Phys. 44 (10), 3888–3894.
Williams, S.R., Philipse, A.P., 2003. Random packings of spheres and spherocylinders simulated by mechanical contraction. Phys. Rev. E 67 (5), 051301.
Wouterse, A., 2008. Random Packing of Colloids and Granular Matter. Utrecht University.
Wouterse, A., Williams, S.R., Philipse, A.P., 2007. Effect of particle shape on the density and microstructure of random packings. J. Phys. Condens. Matter 19 (40), 406215.
Wouterse, A., Luding, S., Philipse, A.P., 2009. On contact numbers in random rod packings. Granul. Matter 11 (3), 169–177.
Wuest, S.B., 2015. Seasonal variation in soil bulk density, organic nitrogen, available phosphorus, and pH. Soil Sci. Soc. Am. J. 79 (4), 1188–1197.
Xu, L., He, N., Yu, G., 2016. Methods of evaluating soil bulk density: Impact on estimating large scale soil organic carbon storage. Catena 144, 94–101.
Xu, W., Zhang, K., Zhang, Y., Jiang, J., 2022. Packing fraction, tortuosity, and permeability of granular-porous media with densely packed spheroidal particles: monodisperse and polydisperse systems. Water Resour. Res. 58 (2), e2021WR031433.
Yang, R., Zou, R., Yu, A., 2000. Computer simulation of the packing of fine particles. Phys. Rev. E 62 (3), 3900.
Yang, R., Zou, R., Yu, A., 2003. Effect of material properties on the packing of fine particles. J. Appl. Phys. 94 (5), 3025–3034.
Yang, R., Zou, R., Dong, K., An, X., Yu, A., 2007. Simulation of the packing of cohesive particles. Comput. Phys. Commun. 177 (1–2), 206–209.
Yerazunis, S., Cornell, S., Wintner, B., 1965. Dense random packing of binary mixtures of spheres. Nature 207 (4999), 835–837.
Yu, A., Standish, N., 1988. An analytical—parametric theory of the random packing of particles. Powder Technol. 55 (3), 171–186.
Yuan, Y., Jiao, Y., Wang, Y., Li, S., 2021. Universality of jammed frictional packing. Phys. Rev. Res. 3 (3), 033084.
Yvan, C., Stéphane, S., Stéphane, C., Pierre, B., Guy, R., Hubert, B., 2012. Role of earthworms in regenerating soil structure after compaction in reduced tillage systems. Soil Biol. Biochem. 55, 93–103.
Zhou, Z.-Y., Zou, R.-P., Pinson, D., Yu, A.-B., 2011. Dynamic simulation of the packing of ellipsoidal particles. Ind. Eng. Chem. Res. 50 (16), 9787–9798.
Zong, C., 2008. Sphere Packings. Springer Science & Business Media.